TKK Dissertations 68
Espoo 2007

STUDIES ON PASSIVE AND ACTIVE ION-EXCHANGED GLASS WAVEGUIDES AND DEVICES

Doctoral Dissertation

Sanna Yliniemi

Helsinki University of Technology
Department of Electrical and Communications Engineering
Micro and Nanosciences Laboratory

TKK Dissertations 68
Espoo 2007

STUDIES ON PASSIVE AND ACTIVE ION-EXCHANGED GLASS WAVEGUIDES AND DEVICES

Doctoral Dissertation

Sanna Yliniemi

Dissertation for the degree of Doctor of Science in Technology to be presented with due permission of the Department of Electrical and Communications Engineering for public examination and debate in Auditorium TU2 at Helsinki University of Technology (Espoo, Finland) on the 4th of May, 2007, at 12 noon.

Helsinki University of Technology
Department of Electrical and Communications Engineering
Micro and Nanosciences Laboratory

Teknillinen korkeakoulu
Sähkö- ja tietoliikennetekniikan osasto
Mikro- ja nanotekniikan laboratorio

Distribution:
Helsinki University of Technology
Department of Electrical and Communications Engineering
Micro and Nanosciences Laboratory
P.O. Box 3500
FI - 02015 TKK
FINLAND
URL: http://www.micronova.fi/units/mns/
Tel. +358-9-451 3167
Fax +358-9-451 3128
E-mail: sanna.yliniemi@tkk.fi

ISBN 978-951-22-8755-0
ISBN 978-951-22-8756-7 (PDF)
ISSN 1795-2239
ISSN 1795-4584 (PDF)
URL: http://lib.tkk.fi/Diss/2007/isbn9789512287567/

TKK-DISS-2294

Otamedia Oy
Espoo 2007

ABSTRACT OF DOCTORAL DISSERTATION

HELSINKI UNIVERSITY OF TECHNOLOGY
P. O. BOX 1000, FI-02015 TKK
http://www.tkk.fi

Author Sanna Yliniemi

Name of the dissertation

Studies on passive and active ion-exchanged glass waveguides and devices

Date of manuscript 19th January 2007	Date of the dissertation 4th May 2007
Article dissertation (overview + original articles)	Number of pages 88+46

Department	Electrical and Communications Engineering
Laboratory	Micro and Nanosciences Laboratory
Field of research	Photonics
Opponent	Dr. Norbert Fabricius
Supervisor	Prof. Seppo Honkanen

Abstract

In this work, new techniques for planar lightwave circuits utilizing silver-sodium ion exchange are explored and developed. Self-diffusion coefficient of Ag^+ ions and the ratio of the self-diffusion coefficients of Ag^+ and Na^+ ions are extracted for electric field assisted thin-film ion exchange in Schott IOG-1 phosphate glass. These are used to find the fabrication parameters for singlemode channel waveguides operating at 1550 nm wavelength region used in telecommunication networks. Birefringence properties of buried molten salt ion-exchanged waveguides are explored. It is shown that waveguides with zero birefringence can be obtained by properly adjusting the thermal annealing time. The effect of waveguide mask opening width on waveguide birefringence is investigated. Low birefringence, 10^{-5} or below, is demonstrated for both the even and odd mode.

Photosensitivity properties of both undoped and Er-Yb-codoped IOG-1 glass are studied. A new approach to fabricate waveguide Bragg gratings through UV exposure in IOG-1 glass is presented. High quality waveguide Bragg gratings with reflectivity of the order of 80% are demonstrated in undoped IOG-1 glass. Waveguide Bragg gratings with lower reflectivity ($R \sim 15\%$) are fabricated in Er-Yb-codoped IOG-1 glass. A singlemode waveguide laser utilizing this kind of a narrowband UV-written waveguide Bragg grating in hybrid IOG-1 glass is demonstrated. Also, the results of a material study of the effect of UV light exposure on this phosphate glass are presented.

In addition, multimode short cavity waveguide laser cavities are designed and fabricated for high repetition rate pulsed lasers. The possibility to utilize these waveguide lasers in mode-locking and/or Q-switching applications is analyzed.

Keywords ion exchange, waveguide, waveguide laser, phosphate glass, photosensitivity, Bragg grating

ISBN (printed)	978-951-22-8755-0	ISSN (printed)	1795-2239
ISBN (pdf)	978-951-22-8756-7	ISSN (pdf)	1795-4584

Publisher TKK Micro and Nanosciences Laboratory

The dissertation can be read at http://lib.tkk.fi/Diss/2007/isbn9789512287567/

VÄITÖSKIRJAN TIIVISTELMÄ

TEKNILLINEN KORKEAKOULU
PL 1000, 02015 TKK
http://www.tkk.fi

Tekijä Sanna Yliniemi

Väitöskirjan nimi

Passiiviset ja aktiiviset ionivaihdetut lasivalokanavat ja komponentit

Käsikirjoituksen jättämispäivämäärä 19.1.2007	Väitöstilaisuuden ajankohta 4.5.2007
Yhdistelmäväitöskirja (yhteenveto + erillisartikkelit)	Sivumäärä 88+46

Osasto	Sähkö ja tietoliikennetekniikan osasto
Laboratorio	Mikro- ja nanotekniikan laboratorio
Tutkimusala	Fotoniikka
Vastaväittäjä	Dr. Norbert Fabricius
Työn valvoja	Prof. Seppo Honkanen

Tiivistelmä

Tässä työssä tutkittiin ja kehitettiin uusia menetelmiä integroidun optiikan piireihin hopea-natrium ionivaihtotekniikkaa hyödyntäen. Diffuusioparametrit sähkökenttäavusteiselle hopeakalvo-ionivaihdolle Schott IOG-1-lasissa iteroitiin vertaamalla prismakytkennän avulla mitattua taitekerroinprofiilia teoreettisesti mallitettuun taitekerroinprofiiliin. Näitä parametrejä voidaan käyttää yksimuotoisten valokanavien valmistamiseen 1550 nm-aallonpituusalueella. Työssä tutkittiin myös haudattujen suolasulasta ionivaihdon avulla valmistettujen valokanavien kahtaistaittavuutta. Haudatuissa valokanavissa voidaan saavuttaa erittäin alhainen kahtaistaittavuus valitsemalla oikea aika lämpökäsittelylle. Valokanavan leveyden vaikutus kahtaistaittavuuteen oli keskeisellä sijalla. Valokanavista mitattu kahtaistaittavuus sekä perusmuodolle (symmetrinen) että toiselle (antisymmetrinen) muodolle on erittäin alhainen ($<10^{-5}$).

Työssä tutkittiin myös passiivisen ja Er-Yb-seostetun IOG-1-lasin fotosensitiivisyyttä ultraviolettivalolle. Työssä esitetään uusi menetelmä valmistaa Braggin hiloja valokanaviin UV-valon avulla. Passiiviselle lasille valmistetuista Braggin hiloista mitattiin korkea heijatus (noin 80%). Er-Yb-seostetulle substraatille valmistetuista hiloista mitatut heijastukset ovat alhaisempia (noin 15%). Yksimuotoisen valokanavalaserin toiminta demonstroitiin hybridilasilla hyödyntäen substraatin passiiviselle osalle UV-valon avulla valmistettua Braggin hilaa. Työssä tutkittiin myös UV-valon fosfaattilasiin aiheuttamia muutoksia, ja pohdittiin näiden muutosten yhteyttä fotosensitiivisyyden alkuperään.

Lisäksi tässä työssä suunniteltiin ja valmistettiin monimuotoisia, lyhyitä valokanavalaserkaviteetteja nopealla taajuudella toimiviin pulssitettuihin lasereihin. Mahdollisuutta käyttää näitä laserkaviteetteja muotolukituksessa tai Q-kytkennässä tutkittiin.

Avainsanat ionivaihto, valokanava, valokanavalaseri, fosfaattilasi, fotosensitiivisyys, Braggin hila

ISBN (painettu)	978-951-22-8755-0	ISSN (painettu)	1795-2239
ISBN (pdf)	978-951-22-8756-7	ISSN (pdf)	1795-4584

Julkaisija Teknillinen korkeakoulu, Mikro- ja nanotekniikan laboratorio

Luettavissa verkossa osoitteessa http://lib.tkk.fi/Diss/2007/isbn9789512287567/

Preface

This Thesis has been carried out in Micro and Nanosciences Laboratory at Helsinki University of Technology. The experimental part of the work was conducted in the College of Optical Sciences in Arizona, USA, between 2003 and 2005.

First and foremost, I wish to express my gratitude to my supervisor Prof. Seppo Honkanen for a wealth of ideas and suggestions, and for his constant support throughout the Thesis project. His guidance has been excellent. I would also like to thank Prof. Jacques Albert from the Carleton University, Ontario, Canada. I feel immensely indebted to him for introducing me into the world of photosensitivity, and for providing me the possibility to visit his laboratory in Ottawa.

I would like to thank Prof. Harri Lipsanen, the head of Micro and Nanosciences Laboratory, for creating an enthusiastic athmosphere in the lab. I am grateful to my former supervisor Prof. Matti Leppihalme for his encouragement in the early phase of my Ph.D. studies. I would like to thank also Prof. Turkka Tuomi for his support.

I am grateful to Dr. Ari Tervonen and Dr. Gualtiero NunziConti for their critical review that helped to improve this Thesis a great deal.

There have been numerous people who have greatly advanced my Thesis project, and it seems to be almost impossible to make a complete list of acknowledgements (my apologies for that!). However, I promise to do my best. I would like to thank my colleague and friend Dr. Brian West for his help in theoretical aspects. My colleague Mr. Qing Wang has continued the work with waveguide lasers after my departure from the College of Optical Sciences, and he has been most helpful with measuments and in keeping me up-to-date about new results. Many thanks to Dr. Jose Castro and Prof. David Geraghty for their contribution in birefringence measurements. I am grateful to Mr. Mike Morrell for his support and inspiration in somewhat

chaotic but always mesmerizing optics measurements. Thanks to Ms. Albane Laronche for her excellent instruction in the photosensitivity lab in Ottawa and to Ms. Elena Temyanko for providing me silver sputterings and mirrors. I feel indebted to Dr. Olli Nordman for keeping the clean room state-of-the-art and for his support. Mr. Aapo Lankinen has been most patient and helpful with the endless number of computer problems I encountered while finishing the Thesis. Thanks to Ms. Outi Reentilä (she might well be Dr. Reentilä when this book comes out) for the late evening therapy sessions. In addition, I would like to thank all my colleagues and the personnel both in the College of Optical Sciences in Tucson and in Micro and Nanosciences Laboratory in Espoo for making the pursuit of work so much more enjoyable.

Both the Magnus Enrhrooth's foundation and the Support Foundation of Helsinki University of Technology have supported my work in Arizona financially. I am grateful for their generous grants that enabled my 3-year stay in the College of Optical Sciences.

I am grateful to my parents for their love and uncondiotional support. Your help has been priceless! I'm also grateful for the warmth and support I have received from my Grandmas and late Grandpas. My friends, both those I had a chance to learn to know in Tucson and those here in the Old World, thanks for distracting me every once and a while from the solitary exercise of writing. Finally, my special thanks belong to my dear sister Kirsi whose caring and shrewd sense of humor probably spared me from the loony house. Hope to see my name printed in the preface of your Thesis soon!

So long and thanks for all the fish!
(Douglas Adams)

Espoo, January 2007 Sanna Yliniemi

Table of Contents

List of Publications

This thesis consists of an overview and the following publications which are referred to in the text by their Roman numerals.

I S. Yliniemi, J. Albert, and S. Honkanen, *A study of silver film ion exchange properties in phosphate glass*, in Optical Components and Materials IV, Shibin Jiang and Michel J. F. Digonnet, eds., Proceedings of SPIE **6469**, 64690Y (2007), 8 pages.

II S. Yliniemi, S. Honkanen, A. Ianoul, A. Laronche, and J. Albert, *Photosensitivity and volume gratings in phosphate glasses for rare earth doped ion-exchanged optical waveguide lasers*, Journal of the Optical Society of America B **23**, 2470–2478 (2006).

III S. Yliniemi, B. R. West, and S. Honkanen, *Ion-exchanged glass waveguides with low birefringence for a broad range of waveguide widths*, Applied Optics **44**, 3358–3363 (2005).

IV S. Yliniemi, J. Albert, A. Laronche, J. M. Castro, D. Geraghty, and S. Honkanen, *Negligible birefringence in dual-mode ion-exchanged glass waveguide gratings*, Applied Optics **45**, 6602–6606 (2006).

V S. Yliniemi, J. Albert, A. Laronche, Q. Wang, and S. Honkanen, *Silver film ion-exchanged Er-doped waveguide lasers and photowritten waveguide gratings in phosphate glass*, in Integrated Optics and Photonic Integrated Circuits, G. C. Righini, ed., Proceedings of SPIE **6183**, 61830M (2006), 5 pages.

VI S. Yliniemi, J. Albert, Q. Wang, and S. Honkanen, *UV-exposed Bragg gratings for laser applications in silver-sodium ion-exchanged phosphate glass waveguides*, Optics Express **14**, 2898–2903 (2006).

Author's contribution

The author has written the manuscripts for all the publications. She has performed the theoretical modeling and all the experiments for publication I. She has designed and fabricated the samples and performed the UV-Vis measurements and the waveguide Bragg grating characterizations for publication II. Raman measurements and surface profile characterizations were carried out by a coauthor. The author has participated in fabrication of the samples for publications III and IV. She has performed all the measuments for the publication III and most of the measurements for the publication IV. The birefringence modeling in publication III was performed by a coauthor. The author has designed and fabricated all the samples for publications V and VI. She has performed all the measurements for the publication V and most of the measurements for the publication VI. The author has been the main contributor in analysis for the publications I-VI.

1 Introduction

The history of the use of glass dates back over 10 000 years. However, it has been only in the last 50 years its electrical and optical properties have arisen more interest along with an increased understanding of non-crystalline materials. The lack of long-range periodicity makes glass and other amorphous materials more difficult to deal with by conventional solid state theory based on the idea of crystalline lattice structure repeating itself in a regular manner. In spite of this, man has known for a long time how to mold and shape glass into useful forms, and it has been used in various applications including household utencils, decorative items, and windows. Glass properties such as strength, thermal and electrical resistance, and color can be manipulated by controlling the glass composition. Another widely deployed method to control these properties is ion exchange. In this process the cations in glass (Na^+, K^+, Li^+) are exchanged by other cations with the same valence (Ag^+, Rb^+, Cs^+, Li^+, K^+, Tl^+) [1]. The process is diffusion driven (either thermal diffusion or electric field assisted ion migration). Ion exchange is by no means a new method, and not all its major applications relate to tailoring glass properties. It has been used already in ancient Egypt to purify drinking water during pharaoh Ramses II c. 1290 BC. First written references to ion exchange can be found in the Torah (Exodus 15: 23-25). Today, ion exchange is exploited in a wide range of applications from wastewater treatment to food industry [2–4]. Ion exchange is an especially important tool for analytical chemistry where it is utilized in chromatography to separate proteins and enzymes [5].

Due to the transparency of glass at optical wavelengths (from UV to IR), it has been also utilized in numerous optics applications including focusing and diverging light beams (lenses) or in separating different wavelength components (prisms). As optics took huge steps throughout the 20th century, new applications for glass emerged. These include glass laser oscillators and optical transmission fibers, the medium on which present day telecommunication networks are by and large based.

Ion exchange in glass produces a graded refractive index profile. This method has enabled inexpensive fabrication of graded index (GRIN) lenses that are utilized as imaging lenses in small photocopiers and scanners [6], in endoscopes enabling minimally invasive surgery [7], and in collimation optics used in high power diode lasers [8, 9]. Ion exchange can be also used to fabricate low loss channel waveguides for planar lightwave circuits (PLCs) in glass substrates. PLCs are widely applied in telecommunication backbone and metropolitan area networks. These networks are based on Dense Wavelength Division Multiplexing (DWDM) technology in which the transmission capacity of a singlemode optical fiber is multiplied by using several tens of wavelengths around the 1550 nm wavelength. Ion-exchanged channel waveguide components, such as optical add-drop multiplexers/demultiplexers (OADM), are capable of multiplexing/demultiplexing a small amount of channels. In addition to OADMs, ion-exchanged glass waveguides have been exploited in a wide variety of components, such as power dividers, Mach-Zehnder interferometers, ring resonators and multimode intereference (MMI) couplers. The coupling between optical fibers and waveguides benefits from the relatively low refractive index change in ion-exchanged waveguides providing good modematching, and therefore, results in reduced power losses in fiber-to-waveguide connections. Waveguide mode size can be further adjusted by burial and/or through thermal annealing post-bake. In addition, ion-exchanged waveguides have been utilized in sensor applications [10–12].

In this work, I have concentrated on exploring and developing new techniques for planar lightwave circuits utilizing silver-sodium ion exchange. In the experiments, two special kinds of glass substrates have been used: aluminoborosilicate glass (also called BGG31) specially developed for passive ion-exchanged waveguides and phosphate glass (commercial name IOG-1) designed for waveguide laser applications. Phosphate glass can be doped with large amounts of rare earth ions enabling fabrication of optically active components (i.e. components that are able to amplify and emit light). First, I will briefly present the basics of the ion exchange method and the compositions of the glass substrates used in this work. Then, I will explore the theoretical considerations of the electric field assisted thin film ion exchange. The diffusion parameters (the self-diffusion coefficient of Ag^+ ions and the ratio of the self-diffusion coefficients of Ag^+ and Na^+ ions) at the process conditions will be extracted and these will be used to guide the fabrication of singlemode channel waveguides operating at 1550 nm wavelength region commonly used in telecommunication networks. Next, a new approach to fabricate waveguide gratings through UV exposure in phosphate glass will be presented. Results of the material study into the effect

of UV light exposure on phosphate glass will be shown. Thereafter, the effect of ion exchange on waveguide birefringence in BGG31 glass will be studied in detail. In addition, a method to reduce waveguide birefringence will be presented. Then, I will proceed to show two different kinds of laser designs in phosphate glass. The first is a multimode short cavity waveguide laser designed and fabricated to operate as a laser cavity in a high repetition rate pulsed laser. The second is a single mode waveguide laser utilizing a narrowband UV-written waveguide Bragg grating as one of the cavity mirrors. Finally, the results are summarized.

2 Ion exchange

Ion exchange is a method in which an ion (A^+) associated with a solid glass matrix (X^-) is replaced by another ion (B^+) with the same valence:

$$X^-A^+ + B^+ \rightleftarrows X^-B^+ + A^+. \tag{2.1}$$

Ion exchange can take place in glass immersed in a melt containing the cations, referred in this Thesis as a molten salt ion exchange. Alternatively, a thin metal film can be used as an ion source, referred as a thin-film ion exchange. Schematics of both methods are presented in Fig. 2.1.

The first ion-exchanged waveguides were fabricated by Izawa and Nakagome [13] into borosilicate glass utilizing a combined $Tl^+ - Na^+$ and $Tl^+ - K^+$ ion exchange from salt melt. Ion-exchanged waveguides provide several advantages over the other commonly used planar optics waveguides (silicon-on-insulator, InP, GaAs, silica-on-silicon, polymer and $LiNbO_3$ waveguides). These include ease of fabrication combined with low propagation loss, better mode field matching with connecting fibers, resulting in low fiber-to-waveguide/waveguide-to-fiber coupling losses, low birefringence and therefore, low polarization dependent loss (PDL) in PLCs. Due to the diffusion nature of the ion exchange process, it is possible to adjust the mode field size and birefringence through thermal post-bake. A disadvantage with ion-exchanged waveguides is that ion exchange produces a relatively low refractive index difference, and therefore bend losses tend to be higher than in etched semicoductor based waveguides. This means that larger bend radii must be used, which leads to increase in the chip size.

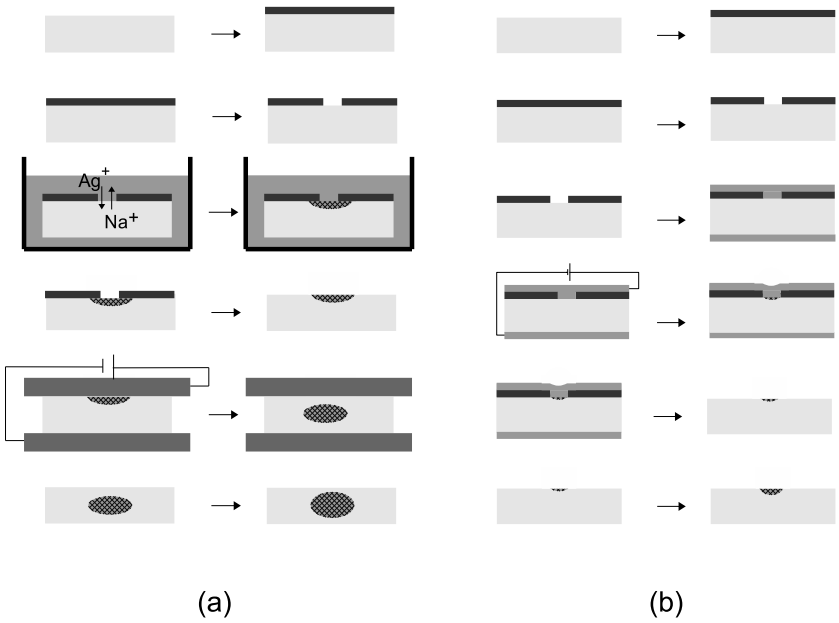

Figure 2.1. A schematic picture of a waveguide fabrication process by ion exchange. (a) Molten salt ion exchange and (b) electric field assisted thin-film ion exchange. From top to bottom in (a) Ti mask deposition, mask patterning, ion exhange, mask removal, field-assisted burial, and thermal annealing and in (b) resist spinning, mask patterning, silver sputtering, electric-field assisted ion exchange, mask removal, and thermal annealing.

2.1 Refractive index change by ion exchange

In ion exchange, a local change in refractive index is produced by replacing alkali-ions by other alkali-ions with the same valence. There are two principal mechanisms contributing to the refractive index change: 1) The differing polarizability and size of the ions participating in the process described by the Lorentz-Lorenz (also known as Clausius-Mossotti) equation [14–16] and 2) induced stress through the photo-elastic effect [14, 17, 18] (described in more detail in Chapter 5).

The Lorentz-Lorenz equation is given by [19]

$$\alpha = \frac{3}{4\pi N}\frac{n^2-1}{n^2+2}, \tag{2.2}$$

where α is the mean polarizability, N is the number of molecules per unit volume, and n is the refractive index.

In Table 2.1, the most common cation pairs used in ion-exchanged glass waveguides, their relative polarizabilities, and sizes are presented. The ion-exchanged waveguides studied in this work are silver-sodium ion-exchanged waveguides fabricated either by molten salt or thin film process.

Table 2.1. Cation pairs commonly used in ion exchange for glass waveguides. r_A and r_B refer to the cation radii given in units of ångtsröm (Å). Polarizability (α) is given units of Å^3.

Salt ion (A)	Glass ion (B)	r_A/r_B	α_A/α_B	Ref.
Li	Na	0.69	0.07	[14]
K	Na	1.35	3.2	[14]
Rb	K	1.12	1.5	[14]
Cs	K	1.24	2.5	[14]
Tl	Na	1.55	12.7	[14]
Tl	K	1.12	3.9	[14]
Ag	Na	1.33	5.6	[1]

$r_{Na} = 0.95$ Å

$\alpha_{Na} = 0.43$ Å^3

2.2 Glass substrates

The basic building blocks of oxide glasses are SiO_2, B_2O_3, GeO_2, P_2O_5, and As_2O_3 tetrahedras [15]. These oxides with strong bonds are called network formers. Glass strength can be enhanced by introducing into the glass matrix so called network intermediates, such as ZnO and PbO. Though network intermediates cannot form glass matrix by themselves, they contribute to the glass strength. Finally, glasses can be tailored to have desired properties by adding network modifiers, such as Na_2O, CaO, and K_2O [15].

In this work, the emphasis is put on two special glasses: 1) Aluminoborosilicate glass, BGG31, and 2) commercially available Schott IOG-1 phosphate glass.

2.2.1 BGG31 glass

Aluminoborosilicate glass BGG31 was specifically developed to fulfill the requirements of ion-exchanged waveguides in passive (i.e. undoped) glass [20].

The glass composition of BGG31 is presented in Table 2.2. The glass network is formed by SiO_2 and B_2O_3 tetrahedras. The waveguides fabricated in this glass feature low intrinsic losses and low birefringence. In addition to sodium ions (high mobility in glass), fluoride ions are introduced to the BGG31 glass. In general, Na_2O decreases the chemical durability and the thermal shock resistance of the glass, and in order to compensate for this side effect, aluminium oxide (Al_2O_3) is incorporated into the glass matrix.

Table 2.2. Glass composition of BGG31 aluminoborosilicate glass [21].

Element	atomic %
O	58.3
Si	17.6
Al	7.1
Na	6.8
B	6.0
F	4.2
As	0.06
K	< 0.01

2.2.2 Schott IOG-1 glass

Phosphate glass is favored in short fiber and waveguide amplifiers and lasers due to the high solubility of rare earth ions without a significant lifetime reduction of the upper amplifier/laser level [22]. This enables high gain values in short cavity lengths and small mode volumes. Commercially available Schott IOG-1 phosphate glass was used in this work to realize short cavity waveguide lasers. The composition of Schott IOG-1 glass is presented in Table 2.3. Phosphate glass matrix is formed by P-tetrahedras with sp^3 orbitals connecting to oxygen atoms through covalent bonds linking with other P-tetrahedras or terminal oxygens (the fifth electron is promoted to 3d orbital where strong π-bonding molecular orbitals are formed with oxygen 2p electrons) [23]. A relatively high amount of aluminium oxide is added to IOG-1 glass to increase durability since phosphate glass is sensi-

tive to surface damage during the ion exchange process [24]. Rare earth ions (Nd^{3+}, Er^{3+}, Yb^{3+}) are added in various combinations in order to obtain the desired spectral properties (more about this in Chapter 6). In the case of undoped phosphate glass, optically passive lanthanoid oxide (La_2O_3) is added instead of other rare earth oxides in order to keep glass properties similar to the doped phosphate glass. Lanthanoid oxide also increases durability.

Table 2.3. Glass composition of IOG-1 phosphate glass [24].

	mol%
P_2O_5	60
Na_2O	24
Al_2O_3	13
R_2O_3	3

R=$\sum$ rare earths

3 Ion-exchanged glass waveguides

3.1 Diffusion equation for electric field assisted binary ion exchange

In electric field assisted binary ion exchange, the effect of both thermal diffusion and ion migration due to the force caused by the driving electric field **E** must be taken into account.

In diffusion, the ion flux (written here as a lower case letter vector **j**, so not to be confused with current density **J**) is proportional to the concentration gradient according to Fick's first law:

$$\mathbf{j} = -D\nabla c, \tag{3.1}$$

where c is the ionic concentration and the proportionality constant D is the self-diffusion coefficient ($D = \delta\bar{x}^2/2t$, where $\delta\bar{x}^2$ is a root mean-square displacement at the time t).

The ion drift flux due to the force (**F**) is

$$\mathbf{j} = \mathrm{c}\mu\mathbf{F}, \tag{3.2}$$

where μ is the ionic mobility ($\mu = \tau/m$, where τ is the average time between collisions with other ions/molecules and m is the mass of the ion). By substituting the force caused by the electric field ($\mathbf{F} = \mathrm{q}\mathbf{E}$) and by using the Einstein relation for the self-diffusion coefficient and the ion mobility ($D = \mu kT$, where k is Boltzmann's constant and T is the temperature), the ion flux due to migration is given by

$$\mathbf{j} = \mathrm{Dcq}\mathbf{E}/\mathrm{fkT}, \tag{3.3}$$

where q is the electric charge of the ion. A correlation factor f has been included in order to take into account the different nature of ionic mobility in diffusion (Eq. 3.1) and in ion migration due to the electric field (Eq. 3.2) [25, 26].

The total ion flux for participating ions A and B in ion exchange is given by adding the contributions from the diffusion and the ion migration:

$$\mathbf{j}_\mathrm{A} = -\mathrm{D_A}\nabla \mathrm{c_A} + \mathrm{c_A D_A e}\mathbf{E}/\mathrm{fkT}, \tag{3.4}$$

$$\mathbf{j}_\mathrm{B} = -\mathrm{D_B}\nabla \mathrm{c_B} + \mathrm{c_B D_B e}\mathbf{E}/\mathrm{fkT}. \tag{3.5}$$

In Eqs. (3.4) and (3.5), ions A and B are considered to be monovalent with a positive charge e. The total concentration c_0 of the mobile ions in glass is

$$c_A + c_B = c_0. \tag{3.6}$$

The conservation of charge requires that the total charge in the glass stays constant during the ion exchange process giving

$$\nabla\left(c_A + c_B\right) = 0. \tag{3.7}$$

The total ion flux $\mathbf{j}_0$ equals to

$$\mathbf{j}_0 = \mathbf{j}_\mathrm{A} + \mathbf{j}_\mathrm{B}. \tag{3.8}$$

By inserting Eqs. (3.4) and (3.5) into Eq. (3.8), and by making use of Eqs. (3.6) and (3.7), the electric field in the glass is obtained:

$$e\mathbf{E}/\mathrm{fkT} = \frac{(\mathrm{M}-1)\nabla \mathrm{c_A} + \mathrm{M}\mathbf{j}_0/\mathrm{D_A}}{\mathrm{c_A}(\mathrm{M}-1) + \mathrm{c_0}}, \tag{3.9}$$

where M is the ratio of self-diffusion coefficients, $M = D_A/D_B$. The flux $\mathbf{j}_\mathrm{A}$ can now be written as:

$$\mathbf{j}_\mathrm{A} = \frac{-\mathrm{D_A c_0}\nabla \mathrm{c_A} + \mathrm{M c_A}\mathbf{j}_0}{\mathrm{c_A}(\mathrm{M}-1) + \mathrm{c_0}}. \tag{3.10}$$

The change in concentration of ions A with time is obtained by using Fick's second law:

$$\frac{\partial c_A}{\partial t} = -\nabla \cdot \mathbf{j}_\mathrm{A}. \tag{3.11}$$

In order to keep the final diffusion equation simple, the relative ion fluxes, $\mathbf{J} = \mathbf{j}_\mathrm{A}/\mathrm{c}_0$, and $\mathbf{J}_0 = \mathbf{j}_0/\mathrm{c}_0$, and the relative ion concentration, $C = c_A/c_0$, will be used. After performing the derivations required by Eq. (3.11), the diffusion equation is given by

$$\frac{\partial C}{\partial t} = \frac{D\nabla^2 C}{C(M-1)+1} - \frac{D(M-1)(\nabla C)^2 + M\mathbf{J}_0 \cdot \nabla \mathrm{C}}{[C(M-1)+1]^2}. \tag{3.12}$$

In certain specific cases it is enough to solve the time-evolution of Eq. (3.12) in only one dimension. In such cases, the Crank-Nicolson method [27] can be applied. This method of solving the time-evolution of the one-dimensional diffusion equation given by

$$\frac{\partial C}{\partial t} = \frac{D\frac{\partial^2 C}{\partial x^2}}{C(M-1)+1} - \frac{D(M-1)\left(\frac{\partial C}{\partial x}\right)^2}{[C(M-1)+1]^2} + \frac{M\mathbf{J}_0 \cdot \frac{\partial \mathrm{C}}{\partial \mathrm{x}}}{[C(M-1)+1]^2} \tag{3.13}$$

is presented in more detail in publication I.

3.2 Boundary conditions

Boundary conditions for the electric field assisted diffusion equation (3.12) depend on the ion exchange method.

In molten salt ion exchange, constant boundary conditions apply:

$$C = \begin{cases} C_s & \text{(surface in contact with a salt melt)} \\ 0 & \text{(other surfaces)} \end{cases}.$$

The constant value, C_s, depends on the concentrations of the participating ions in the salt melt (determined from regular solution theory) [28, 29]. In $\mathrm{Ag}^+ - \mathrm{Na}^+$ ion exchange, the value for the constant C_s is 1 for pure $\mathrm{AgNO_3}$ and 0 for pure $\mathrm{NaNO_3}$ [29]. The above equation requires that the equilibrium conditions are achieved rapidly.

Thin film $\mathrm{Ag}^+ - \mathrm{Na}^+$ ion exchange can be considered as an electrolysis process in which positively charged Ag^+ ions drift from a silver anode through a solid electrolyte (glass) towards the silver cathode [25, 29]. The ion flux ($\mathbf{J}_\mathrm{Ag}$) is perpendicular to the surface chosen here to be along y-direction.

The surface boundary condition is given therefore by:

$$\mathbf{J}_{\mathrm{Ag}} = \mathbf{J}_0. \tag{3.14}$$

The Ag^+ ion flux on other surfaces is zero. By substituting Eq. (3.14) into Eq. (3.10), the boundary conditions for a thin film $Ag^+ - Na^+$ ion exchange can be presented in a more useful form as:

$$\frac{\partial C}{\partial y} = \begin{cases} J_0 \left(C_{Ag} - 1\right)/D & \text{(surface in contact with a silver thin film source)} \\ 0 & \text{(other surfaces)} \end{cases}.$$

3.3 Diffusion parameter extraction and channel waveguide mode profiles

In the following, the results of parameter extraction and the channel waveguide mode profiles presented in publication I are briefly reviewed. In order to find out the diffusion coefficient and the mobility required for modeling the light propagation properties in a waveguide, an approach similar to Honkanen and Tervonen [30] was adopted. First, an IOG-1 phosphate glass sample was coated by a 500 nm-thick silver layer. Silver ions were driven with an electric field assisted ion exchange into glass in a temperature controlled oven. During the process, the silver ion current and the temperature were monitored with a multimeter and a thermocouple. Ion exchange was performed at T = 95°C with a voltage of 200 V applied over a 1.5 mm thick substrate. After ion exchange, the residual silver film was removed in NH_4OH/H_2O_2 wet etch. The effective indices of the modes propagating in a slab waveguide were measured by prism coupling and the refractive index profile was constructed according to Chiang's recursive inverse Wentzel-Kramers-Brillouin (IWKB) algorithm [31]. Thereafter, Ag^+-ion concentration profile was simulated via the Crank-Nicolson method by varying the self-diffusion coeffient (D) and the ratio of self-diffusion coefficients (M) in Eq. (3.13) until agreement with the refractive index profile was achieved. The same procedure was also applied in the case of an annealed slab waveguide but this time with a zero current in Eq. (3.13) since no electric field was applied during the thermal post-bake.

In Table 3.1, the diffusion parameters at process conditions deduced by combining the results from the time-evolution of the diffusion equation (3.13) and the results from the IWKB analysis are presented. It was concluded

that the self-diffusion coefficient and the ratio of self-diffusion coefficients in IOG-1 glass are of the order of 5×10^{-18} m^2/s and 0.7 at ion exchange conditions used to fabricate two-dimensional waveguides (T = 95°C, U = 200 V) and 3×10^{-16} m^2/s and 0.7 at conditions applied during the thermal post-bake (T = 230°C, U = 0 V).

Table 3.1. Self-diffusion coeffient (D_{Ag}) and the ratio of self-diffusion coefficients ($M = D_{Ag}/D_{Na}$) at different process conditions.

T [°C]	U [V]	D_{Ag} [m^2/s]	M
95	200	5×10^{-18}	0.7
230	0	3×10^{-16}	0.7

Using the estimates given in Table 3.1, waveguide mode profiles were theoretically calculated from Eq. (3.12) by the finite difference time domain method using a software developed previously by our research group. The theoretically calculated and the measured mode profiles are presented in Figs. 3.1 and 3.2 for a mask opening width of 3 μm at signal (1535 nm) and pump (980 nm) wavelengths. Ellipticity and the modeled and measured mode profile dimensions defined at $\frac{1}{e^2}$-intensity point are presented in Tables 3.2 and 3.3.

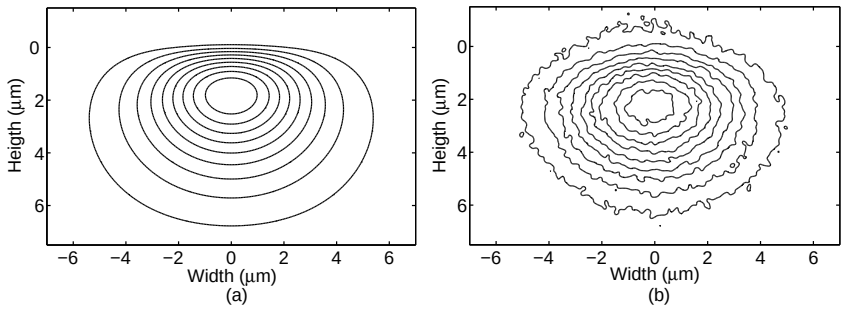

Figure 3.1. Theoretical (a) and measured (b) mode profiles at signal (1535 nm) wavelength. Waveguide mask opening width is equal to 3 μm. The intensity difference between the isocontours is 10% of maximum intensity.

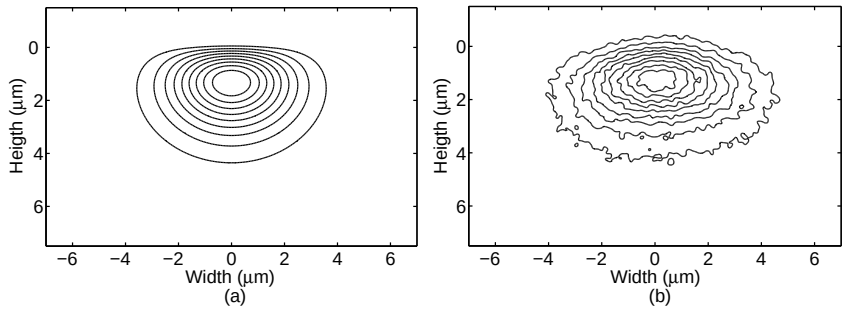

Figure 3.2. Theoretical (a) and measured (b) mode profiles at pump (980 nm) wavelength. Waveguide mask opening width is equal to 3 μm. The intensity difference between the isocontours is 10% of maximum intensity.

Measured mode profiles appear to have a slightly elliptic shape with increasing ellipticity as a function of a mask opening width while the theoretical mode profiles show the smallest ellipticity for the waveguide with a mask opening width of 3 μm at signal wavelength. Besides this one exception, theoretically modeled waveguides show increasing ellipticity with a mask opening width.

It can be also observed that the theoretically calculated mode profile dimensions for the narrowest mask opening width are larger than those for the wider mask opening widths (at 1535 nm). This can be associated with the fact that the waveguide with the narrowest mask opening width (2 μm) has the lowest amount of Ag^+ ions, therefore producing the weakest mode confinement and furthermore, a relatively large mode size. The modes propagating in other waveguides are more confined resulting in smaller mode profile dimensions. The discrepancies between the theoretically modeled and the measured mode profiles can be explained by the inaccuracies in the lithography process that is especially pronounced in the case of the mask opening width of 2 μm. At signal wavelength the waveguides with mask opening widths of 2 μm and 3 μm are single mode while the rest of the waveguides are multimode. At pump wavelength, all the waveguides are multimode. The larger measured mode dimensions in the lateral direction compared with the theoretical mode profiles at pump wavelength can be explained by the difficulty in coupling light exclusively to the fundamental propagating mode.

Table 3.2. Mode profile dimensions at different mask opening widths at (signal) wavelength of 1535 nm.

Mask opening width [μm]		Width [μm]	Height [μm]	Ellipticity
2	measured	8.9	6.4	0.69
2	modeled	11.0	7.0	0.77
3	measured	9.1	6.3	0.72
3	modeled	9.6	6.4	0.75
4	measured	8.0	5.4	0.74
4	modeled	9.1	5.8	0.77
5	measured	9.7	5.7	0.81
5	modeled	9.0	5.4	0.80

Table 3.3. Mode profile dimensions at different mask opening widths at (pump) wavelength of 980 nm.

Mask opening width [μm]		Width [μm]	Height [μm]	Ellipticity
2	measured	5.9	3.8	0.76
2	modeled	7.0	4.7	0.74
3	measured	7.7	4.1	0.85
3	modeled	6.6	4.1	0.78
4	measured	7.7	3.9	0.86
4	modeled	6.5	3.7	0.82
5	measured	8.9	4.0	0.89
5	modeled	6.7	3.7	0.83

4 Photosensitivity of phosphate glass

In 1978, Hill and coworkers discovered photosensitivity of a Ge-doped silica fiber by illuminating the fiber with an Ar-laser light [32]. Light launched into the fiber reflected back at the glass-air interface at the other end of the fiber and formed a standing wave pattern inside the fiber. The refractive index of the fiber was permanently modulated with the same periodicity as the interference pattern. These early experiments aroused little interest in optics community and it was only a decade later when the significance of the fiber photosensitivity was properly understood. In 1987, Stone [33] demonstrated photosensitivity in a number of fibers and in 1989 Meltz *et al.* [34] demonstrated gratings with reflectivity above 50% in a germanosilicate fiber. In the same year, Hand and Russell explained the link between the changes in absorbance at UV-wavelengths and the apparent UV-induced refractive index change at infrared wavelengths through Kramers-Kronig relations [35]. A remarkable improvement in fiber Bragg grating fabrication was achieved when Hill *et al.* and Andersson *et al.* introduced, independently from each other, the phase-mask technique [36, 37]. Phase-mask technique is superior over the earlier grating inscribing methods both in cost and in robustness. Today, fiber Bragg gratings are important components both in erbium doped fiber amplifiers (EDFA) and in wavelength division multiplexing (WDM) devices [38].

In this work (presented in publication II), I have concentrated on studying photosensitivity of both undoped and Er-Yb codoped phosphate glass (IOG-1). Later on, it will be shown that it is possible to write high quality Bragg gratings into undoped IOG-1 glass (see Chapter 7). Somewhat weaker Bragg gratings were fabricated into Er-Yb codoped glass. Experiments studying the UV-induced structural modifications and spectroscopical changes were also carried out. The relation between these UV-induced changes and the

increase of the refractive index at infrared wavelengths is briefly discussed at the end of this chapter.

4.1 Bragg diffraction

Scattering from lattice planes of a crystalline material was first explained by von Laue in 1912. He stated that diffraction beams are produced whenever a reciprocal lattice point coincides with surface of the Ewald sphere [16], or the condition

$$\mathbf{K} = \mathbf{G} \tag{4.1}$$

is met. In the von Laue condition, $\mathbf{K}$ is equal to the difference between the wavevectors $\mathbf{k}$ and $\mathbf{k}_0$, and $\mathbf{G}$ is the reciprocal vector of the crystal lattice. Shortly afterwards, the von Laue condition was re-intepreted by Sir W. L. Bragg. He discovered that diffraction could be understood as a reflection of the incident beam from the lattice planes. The Bragg condition

$$m\lambda = 2d\sin(\theta) \tag{4.2}$$

states that a constructive interference is produced if the path difference between the rays reflecting from the different lattice planes is equal to an integer number of wavelengths (λ) of the incident beam. In Eq. 4.2, d is the distance between the crystal planes and the angle θ is defined as shown in Fig. 4.1 a.

Bragg gratings can be artificially produced in material by introducing a refractive index modulation with a period comparable to the wavelength of the incident beam. Fiber Bragg gratings and photonic crystal materials represent such artificially produced gratings. In case of fiber Bragg gratings it is more convenient to define the angle θ as shown in Fig. 4.1 b. Thus the Bragg condition now becomes:

$$m\lambda_0 = 2n_{eff}\Lambda\cos(\theta), \tag{4.3}$$

where n_{eff} is the effective refractive index of the propagating mode and Λ is the period of the grating. Here, λ_0 is the vacuum wavelength. In the case of normal incidence ($\theta = 0$), Eq. (4.3) reduces to a form given by:

$$m\lambda_0 = 2n_{eff}\Lambda. \tag{4.4}$$

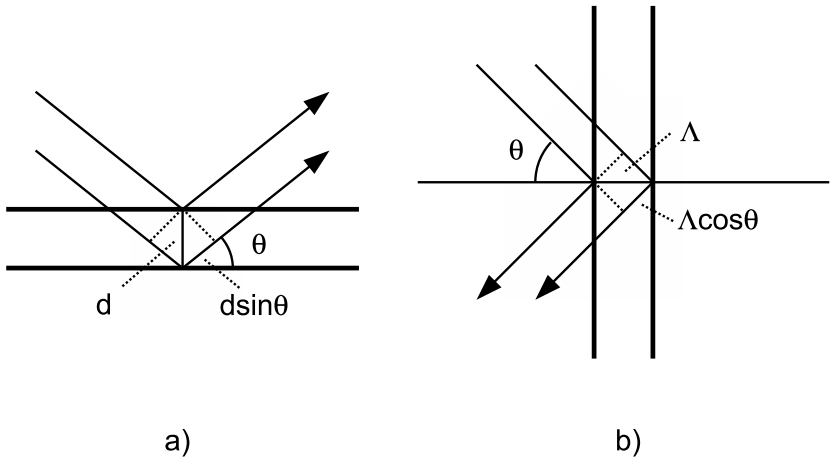

Figure 4.1. Bragg diffraction in a) crystal geometry and b) fiber/waveguide geometry. d refers to the distance between atomic layers in crystal geometry while Λ is the the Bragg period produced by UV-writing in fiber/waveguide Bragg gratings.

Wavelengths satisfying the Bragg condition are reflected by a grating while all the other wavelengths are transmitted. In practical cases, the reflected wavelengths have a bandwidth $\Delta\nu$, the bandwidth being narrower the longer the grating is (for the case of a "weak-grating limit") or the higher the index modulation is (for the case of a "strong grating limit") [39]. Also, the reflected intensity increases as the grating length increases. If the grating period is increased (or decreased) along the fiber axis, a chirped grating is obtained. These kinds of gratings are widely exploited in broadband reflectors and in dispersion compensation.

4.2 Excimer lasers

The term excimer refers to a group of molecules that can exist only in an excited state. These molecules do not have an energy minimum in their ground state and therefore dissociate very quickly in a ground state. Typically, noble gases (Xe, Kr, Ar) and halogens (F, Cl, Br, I) can form excimers. An ionized noble gas ion in an excited state (e.g. Ar^* or Kr^*) attracts a negatively ionized halogen ion (e.g. F^-) and forms an excimer molecule in an exothermic, or energy releasing, reaction while the reaction with ions in

their ground state would have been endothermic, or energy requiring, and therefore is not favored by nature. The lifetime of the bound state is of the order of several nanoseconds while the unbound molecule dissociates in approximately one vibrational period, or 10^{-13} s [40, 41]. The almost nonexistent ground state lifetime of an excimer molecule makes it a good choice of material for two-level laser applications. Indeed, very high powers can be extracted from excimer lasers. Due to the relatively short upper state lifetime, excimer lasers operate best in a pulsed state. They are pumped electronically by electron beams capable of ionizing noble gas and halogen atoms. Excimer lasers typically emit at ultraviolet wavelengths, a wavelength range not very well covered by other gain media. Short upper state lifetime also results in a high spontaneous emission rate and in relatively poor coherence properties.

The excimer laser systems used in this work for writing waveguide Bragg gratings were argon fluoride (ArF) with a stimulated emission at 193 nm and krypton fluoride (KrF) with a stimulated emission at 248 nm. When the laser was run with an ArF gas mixture, unstable resonator optics were used, yielding pulses with an energy of 100 mJ. With the KrF gas mixture, stable resonator optics were used, delivering pulses with an energy up to 400 mJ. Unstable resonator optics provide increased spatial coherence due to a much smaller front reflector area, resulting in fewer oscillating spatial modes. This allows tighter focusing of the laser beam output, which partially compensates for the lower gain obtained from the unstable resonator. However, the pulse length for 248 nm is close to 20 ns while it is only 14 ns for 193 nm, therefore the use of 193 nm gives 40% more peak power at the same pulse energy.

4.3 Phase mask technique

Fiber Bragg grating fabrication was simplified considerably by the introduction of the phase mask technique [36, 37]. In this technique, a piece of silica glass with an etched surface-relief grating on one side of the substrate is placed in close proximity with a fiber (or, as in this work, with the glass substrate). This acts as a thin transmission grating operating in Raman-Nath regime. The grating produces multiple waves diffracted at angles θ_q obtained from the grating equation [42]

$$\sin\theta_q = q\frac{\lambda}{\Lambda}, \tag{4.5}$$

where λ is the wavelength of the incident light, Λ is the period of the surface-relief grating, and q is the order of the diffraction. The angle θ_q is measured with respect to the incident light. Usually, the phase retardation (phase difference induced by corrugation depth) and the duty cycle of the grating (the ratio between the width of the corrugation and the phase mask period) is designed in such a way that the power to the other diffraction orders - besides the orders ± 1 - is minimized [36, 42, 43]. The two plane waves with diffraction orders -1 and $+1$ form an interference pattern with a periodicity which is half of that of the phase mask peridiocity, and this periodicity is independent on the illumination wavelength [44].

A small drawback of the phase mask method is that the corrugation depth for a zero-order nulled operation is wavelength dependent, therefore requiring a different phase-mask for each irradiation wavelength. However, if compared with the internal writing or the holographic technique, the stability and coherence requirements are greatly relaxed enabling the use of high energy excimer lasers [45, 46].

The phase-mask technique has also enabled more complex grating designs, such as apodized gratings used to suppress the sidelobes present in reflection from a grating with a uniform index modulation [39] and the fabrication of chirped gratings used in dispersion compensation [47].

4.4 Mechanisms behind photosensitivity

4.4.1 Color center model

The color center model relates the UV-induced change in absorption ($\Delta\alpha$) at short wavelengths to the increase in refractive index at infrared wavelengths through Kramers-Kronig relations

$$\Delta n\left(\lambda'\right) = \frac{1}{2\pi^2}\mathrm{PP}\int_0^\infty \frac{\Delta\alpha\left(\lambda\right)\mathrm{d}\lambda}{1-\left(\frac{\lambda}{\lambda'}\right)^2}, \tag{4.6}$$

where PP refers to Cauchy's principal value. The color center model was first suggested by Hand and Russell based on their observations of the bleaching of the absorption band around the wavelength of 240 nm [35]. These bands are formed by germanium-oxygen vacancy defects (GODC)

produced during the fiber drawing. A schematic picture of a GODC (a Ge-Si or a Ge-Ge "wrong bond") is depicted in Fig. 4.2. Instead of bonding to another Ge or Si atom through a bridging oxygen atom, the Ge atom is bonded to either Ge or Si atom through an electron. UV-irradiation breaks these "wrong bonds". During the bond breakage the bonding electron is released and this electron can either recombine immediately with GeE' center (Ge atom bonded to three oxygen atoms and to an empty site) or it can diffuse through the glass matrix and eventually be trapped at Ge(1) or Ge(2) center creating $Ge(1)^-$ or $Ge(2)^-$ color centers [46]. A Ge(1) center refers to a Ge atom bonded to four Si atoms through a bridging oxygen and a Ge(2) center refers to Ge atom bonded to three Si atoms and to one Ge-atom through a bridging oxygen. These color centers have absorption bands at 281 nm, 213 nm, and 197 nm, respectively [35, 48]. Several studies have established the validity of the color center model as explaining a major part of the UV-induced index change in Ge-doped silica fibers [49–51]. The color center model was also discovered to be behind the UV-induced index change in phosphorus-doped silica glass [52]. Photosensitization techniques, including hydrogen loading [53], flame brushing [54], boron, tin, germanium, or rare earth codoping [55], and exposure to ArF excimer laser irradiation [56], have been observed to enhance color center formation, and as such can be used to increase the refractive index change at infrared wavelengths.

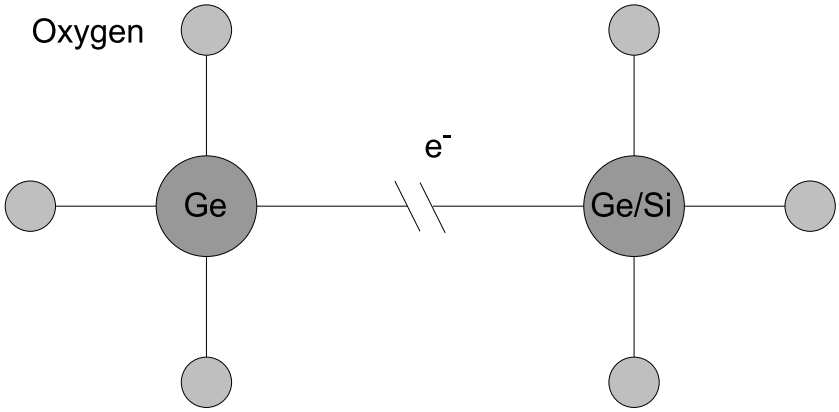

Figure 4.2. A schematic picture of a germanium-oxygen vacancy defect. Instead of a bridging oxygen, germanium atom is linked to another Ge/Si atom through an electron. The electron is released during the irradiation induced bond breakage.

4.4.2 Compaction/densification model

While the UV-induced color center formation has been by and large accepted to be the dominant source of the refractive index change in Ge-doped silica fibers, the discussion of the mechanisms lying behind photosensitivity in other fibers remains more controversial. Another model that has received a lot of attention is the so called compaction or densification model. The irradiation breaks or weakens the bonds in glass causing structural modifications and furthermore, either densification or expansion of material. In this model, the UV-induced volume change (either by densification or expansion) introduces a refractive index change as predicted by the Lorentz-Lorenz relation (See Eq. (2.2) in Chapter 2). The sign of the refractive index change depends on the stress distribution near the surface and the stress-optic coefficients of the glass [17]. Fiori and Devine [57] were the first to observe UV-induced compaction in vitreous amorphous silica. Compaction was assumed to occur through breaking of higher order $a - SiO_2$ ring structures into two or three-member ring structures. After all the ring structures are consumed, further irradiation results in permanent compaction similar to laser ablation. Existence of three member ring structures have been observed in irradiated GeO_2 doped silica fibers in Raman studies performed by Gabriagues and Fevrier [58]. Earlier work by Primak and Kampwirth [59, 60] had already related the refractive index change to radiation-induced compaction in vitreous silica. Compaction was observed in samples irradiated by radiation of ionizing character like neutrons, high-energy electrons, protons, deuterons and gamma-rays. Densification induced refractive index change has also been demonstrated by experiments carried out by Cordier *et al.* [61] and Poumellec *et al.* [62].

Several studies have suggested that the UV-induced index change has a different origin depending on whether the irradiation wavelength of 193 nm or 248 nm is used. Rothchild *et al.* [63] observed that the refractive index in pure silica fiber increased quadratically as a function of intensity when irradiated by 193 nm light, thereby linking the absorption of 193 nm irradiation to a two-photon process. This observation was supported by the experiments performed by Albert *et al.* [64] in defect-free Ge-doped silica fibers at wavelength of 193 nm. Borrelli *et al.* [65] did not consider densification as a major source of UV-induced refractive index increase in samples irradiated by 248 nm, while in samples irradiated by 193 nm light the effect of densification initiated by a two-photon absorption was considered to be more dominant. In fact, they went as far as to state that in oxygen-defect free samples it might be the sole source of the induced refractive index

change. They also pointed out the importance of the thermal history in material densification process [66].

4.5 Undoped (passive) IOG-1 glass

In figure 4.3, the transmission spectra from ultraviolet to near-infrared wavelengths are shown for undoped and Er-Yb codoped IOG-1 glass as well as for ion-exchanged undoped glass. Three things can be immediately observed from Fig. 4.3. First, almost no transmission is observed below wavelengths 230 nm for Er-Yb codoped and ion-exchanged glass, suggesting that absorption at those wavelengths is very high with all the irradiation below 230 nm being absorbed in a thin surface layer. Therefore, for the Er-Yr codoped glass the irradiation wavelength of 248 nm was chosen instead of 193 nm. For undoped glass, however, the irradiation wavelength of 193 nm is a better choice as the transmission at the wavelength of 248 nm is already too high.

First experiments were carried out with undoped substrates in which waveguides were already fabricated. A phase mask with a period of 1015 nm and a length of 9 mm was used. The ArF excimer laser was run at 100 pps (pulses per second) with a fluence of 460 mJ/cm^2. It was observed that a grating with reflectivty between 1% and 12% was obtained after a relatively short irradiation time of 4 min, with further irradiation erasing the grating. Clearly, these low grating reflectivities are not practical for mirrors in lasers applications.

Stronger free-space diffraction efficiencies (measured by illuminating the sample by a He-Ne laser at different angles) were always measured at the sides of the waveguides where Ag^+ concentration is lower suggesting that Ag^+ and Ag^0 species might prevent irradiation from penetrating deep enough into the glass. In view of this, the grating irradiation was carried out with a pristine sample and the waveguides were fabricated only after writing of the grating. The laser was run in ArF mode with a fluence of 300 mJ/cm^2. Reflectance and transmittance spectra of the grating are shown in Fig. 4.4. Reflectance of 44% (calculated from the transmission dip) was reached with only a 4 mm long grating and 5 min exposure time. The measured reflectivity corresponds to an index modulation of 1.0×10^{-4} if a full overlap between the waveguide and grating fringes is assumed (See Eq. 4.8). The value of index modulation obtained from (4.8) corresponds to a value deduced from the free space diffraction measuments (Eq. 4.7).

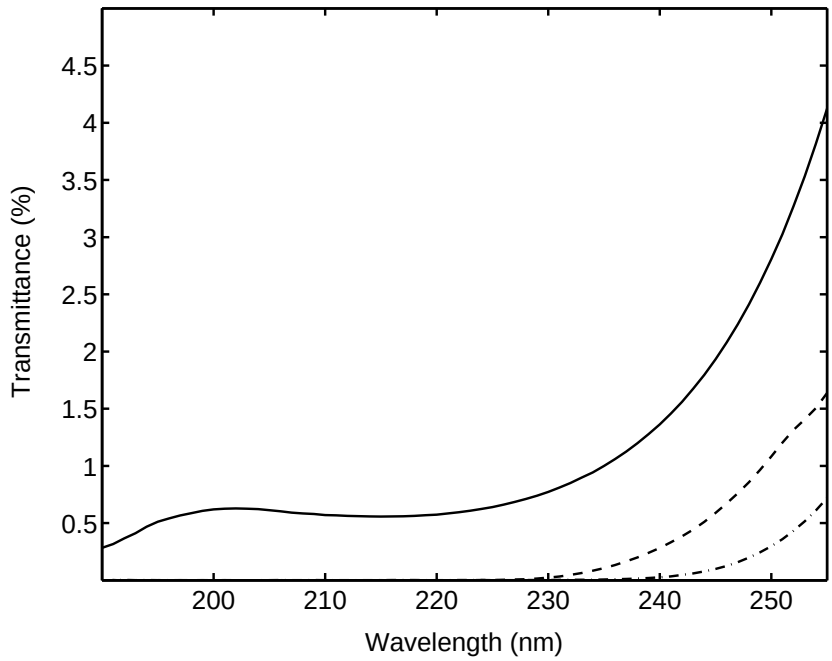

Figure 4.3. UV-Vis transmission spectra for passive IOG-1 (undoped, solid line) and active IOG-1-7 (Er/Yb-codoped, dashed line), and for ion-exchanged passive IOG-1 (dash dotted line) glass substrates. The thickness of the substrates was 1.5 mm.

The amplitude of the refractive index modulation can be estimated if the diffraction efficiency is known [40]. Diffraction efficiency ($\eta = I_{diff}/I_0$) is related to the amplitude of the refractive index modulation (Δn) through equation

$$\eta = \sin^2\left(\pi d \Delta n / (\lambda_0 \cos\theta_{Bi})\right), \tag{4.7}$$

where d is the thickness of the grating, λ_0 is the wavelength of the incident light, and θ_{Bi} is the internal angle relative to the sample perpendicular.

The amplitude of the refractive index modulation and the reflectance (R) are related through equation [39]

$$R = \tanh^2\left(\frac{\pi \Gamma \Delta \mathrm{n}}{\lambda_{\mathrm{Bragg}}} \mathrm{L}\right), \tag{4.8}$$

where R is the reflected power, Γ is the overlap factor between the propagating mode in the waveguide and the grating, λ_{Bragg} is the Bragg wavelength, and L is the grating length.

The reflectance and transmittance spectra are presented in Fig. 4.4. The phase mask period was 1065 nm giving a reflectance peak at 1608 nm in undoped IOG-1 glass. The inspection of the grating before waveguide fabrication revealed that the grating is a volume grating operating in Bragg regime. The reflectance spectrum shows no coupling to the cladding modes. These experiments show that it is possible to write high quality Bragg gratings into passive IOG-1 glass, and reflectances high enough for waveguide laser applications can be achieved simply by increasing the grating length. This kind of a grating was fabricated and tested as a mirror in a waveguide laser cavity in this work (see Chapter 7).

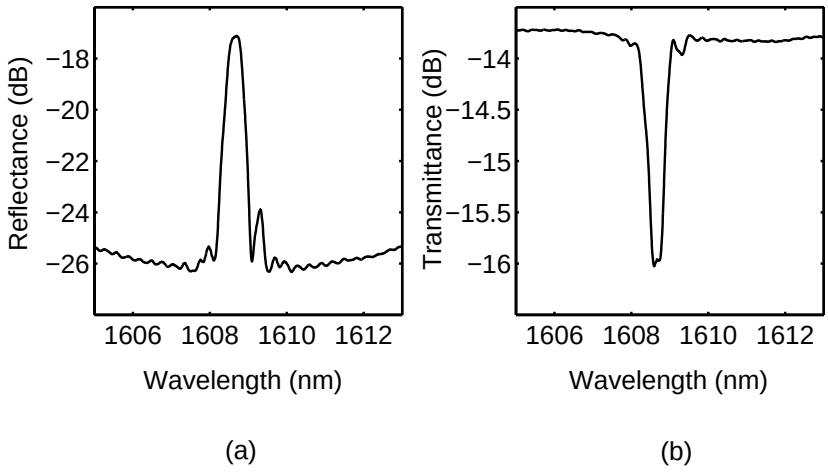

Figure 4.4. (a) Reflectance and (b) transmittance spectra for a waveguide grating in undoped IOG-1 glass. Grating reflectivity is equal to 44%. This value was calculated from the transmission dip.

4.6 Er-Yb-codoped (active) IOG-1 glass

The waveguides in active IOG-1 glass were fabricated only after the grating exposure. UV-writing was performed with a fluence of 250 mJ/cm^2 for 30 min at a wavelength of 248 nm. The highest grating reflectance produced in this way was only 15% with a grating length of 13 mm corresponding to

an index modulation of 1.5×10^{-5}. The polarization dependent wavelength shift of the grating was equal to 0.02 nm corresponding to birefringence of the order of 10^{-4}, as expected for a surface waveguide. The grating operates in Bragg regime, but the index modulation is too low for laser quality gratings. The significantly lower index modulation compared with the one obtained with an ArF laser emitting at 193 nm into undoped glass is most probably due to the combined effect of the poorer coherence properties of the excimer laser system at 248 nm along with the fact that absorption at 248 nm is weaker in Er-Yb codoped glass compared with absorption in undoped glass at 193 nm.

4.7 Material studies of IOG-1 glass

The change in absorbance (absorbance defined as $-(1/l)\log T_i$, where l is the thickness of the material layer and T_i is the transmittance of the layer) due to UV-irradiation at 193 nm and annealing is shown for undoped glass in Fig. 4.5. From this figure, it can be observed that a strong UV-irradiation induced absorbance peak appears at 180 nm in undoped IOG-1 glass, also a broader and weaker peak around 460 nm can be observed. The peak around 180 nm reduces only slightly after thermal annealing (90 min at 230°C) compared with the broader peak around 460 nm. The absorbance changes observed in Er-Yb codoped IOG-1 glass were more moderate as can be seen from Fig. 4.6. A broad peak around 460 nm is again observed, however, there is no sign of a peak or absorption edge at lower wavelengths as in the case of the passive UV-irradiated sample.

Measurements with a Tencor P1 profilometer revealed a volume expansion with an increasing ridge height as a function of an irradiation dose. Ridge height as high as 700 nm was measured after an irradiation dose of 60 kJ/cm^2. Diffraction efficiency (calculated from Eq. (4.7)) increased until the total dose was equal to 40 kJ/cm^2, after which it started to decrease. The ridge height along with the diffraction efficiency as a function of a dose are presented in Fig. 4.7. Interestingly, annealing improved the diffraction efficiency in samples that were originally overdosed while the gratings in the samples with a high diffraction efficiency in the beginning weakened considerably. Raman measurements showed signs of structural changes too. A decrease of 10% in the ratio of the P-O-P (with a bridging oxygen) to the O-P-O (with two terminal oxygens) symmetric stretching modes indicates that the ArF irradiation breaks some chemical bonds and rearranges the network structure of the glass [67, 68]. This suggests that depolymerization

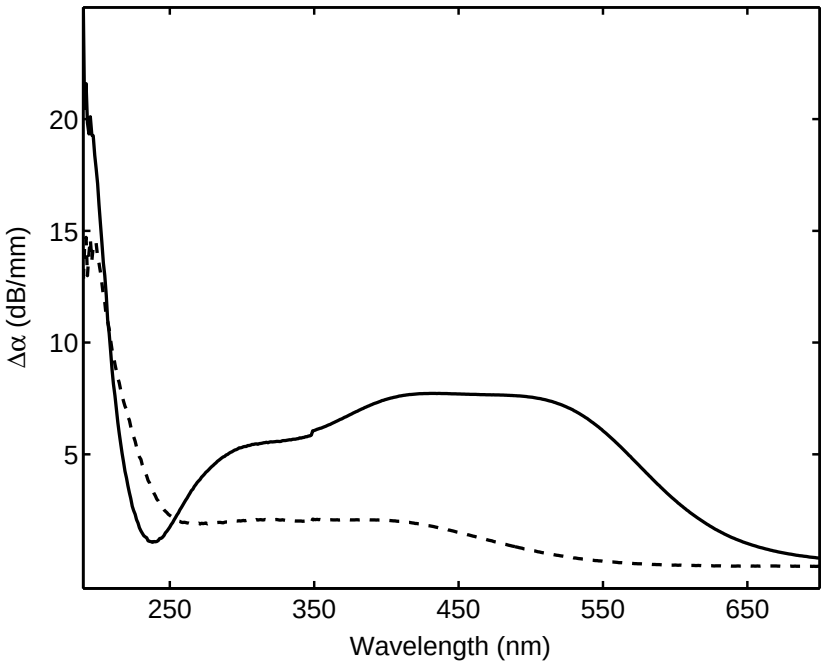

Figure 4.5. Change in absorbance ($\Delta\alpha = -(1/l)\log \mathrm{T_i}$) due to the UV-irradiation and annealing for undoped IOG-1 glass. Solid line refers to the induced absorbance in the UV-irradiated sample and dashed line to the induced absorbance in the UV-irradiated and annealed sample. The thickness of the UV irradiation affected layer was estimated to be 0.3 mm while the total sample thickness was 1.5 mm.

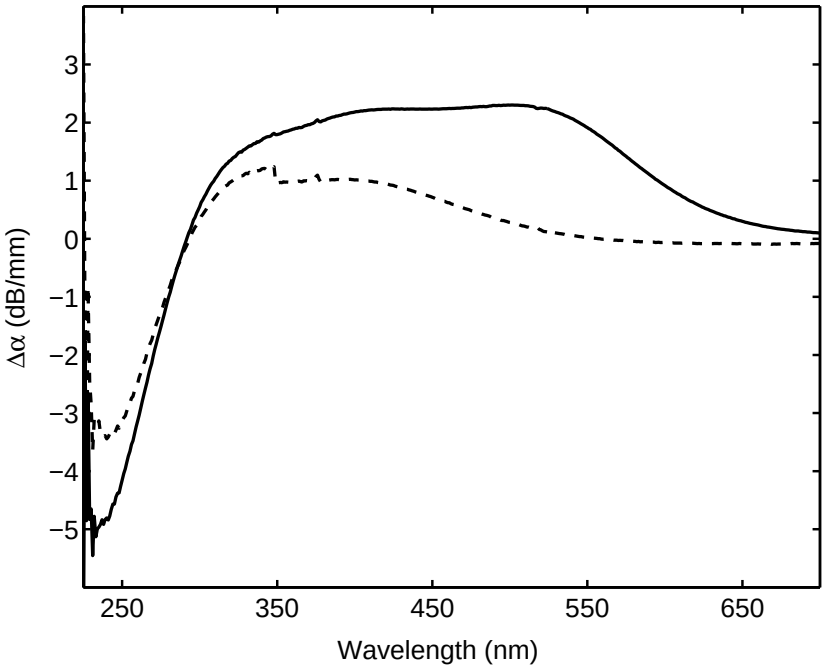

Figure 4.6. Change in absorbance ($\Delta\alpha = -(1/l)\log \mathrm{T_i}$) due to the UV-irradiation and annealing for Er-Yb codoped IOG-1 glass. Solid line refers to the induced absorbance in the UV-irradiated sample and dashed line to the induced absorbance in the UV-irradiated and annealed sample. The thickness of the UV irradiation affected layer was estimated to be 0.3 mm while the total sample thickness was 1.5 mm.

takes place during the irradiation and the phosphate chains in the glass matrix are shortened.

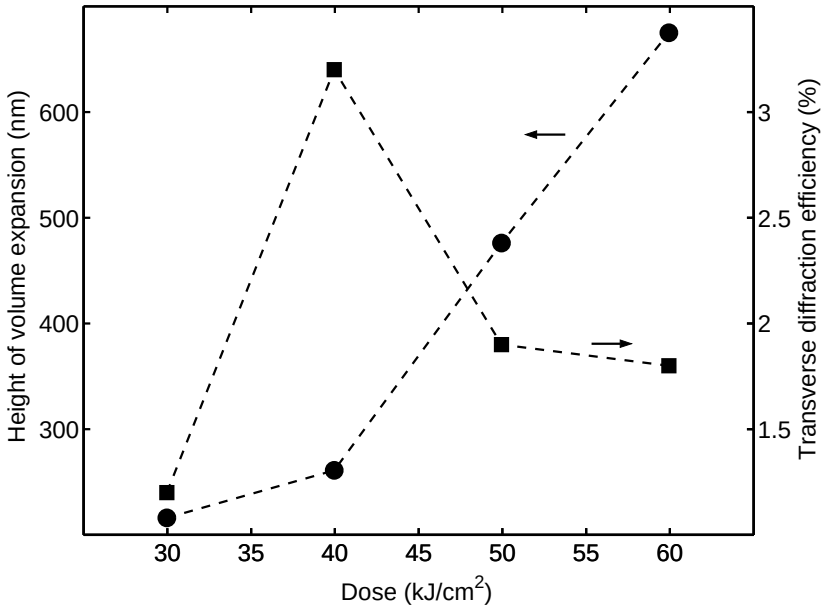

Figure 4.7. Volume expansion height (circles) and diffraction efficiency (squares) as a function of irradiation dose. The dashed lines combining the circles/squares have been plotted for ease of viewing.

In this study, both UV-induced spectral changes and structural modifications were observed. However, the fundamental question about the dominant mechanism behind photosensitivity could not be exclusively answered. Should the material compaction have a more dominant effect, the induced refractive index change should be negative since the stress-optic coefficient of phosphate glass is negative [17, 69] and a volume expansion instead of material densification was observed. Negative index changes produced by irration at 193 nm could be also related to the color center model in a similar manner as in a study by Verhaegen *et al.* [70]. The sign of the index change was not confirmed in this study, so the possibility of a positive refractive index change induced by the color centers should also be considered. The high induced absorption near 190 nm that was observed also after thermal annealing is so far the strongest evidence supporting the color center model. This possibility is also supported by the study by Malo *et al.* [52] in which they observed an increase in refractive index in Ge-free phosphorus-doped silica-glass (flame brushed and hydrogen loaded) when irradiated at 193 nm. The index change was related to the color center formation at wavelengths

below 220 nm. It should be also pointed out that both color centers formed at UV-wavelengths and the structural modifications can contribute to the induced refractive change.

After annealing, UV-induced spectral changes were less permanent in Er-Yb codoped IOG-1 glass and no structural modifications could be detected. However, the UV-induced index modulation in Er-Yb codoped glass was an order of magnitude smaller than in undoped IOG-1 glass. It is probable that the UV-induced changes in Er-Yb codoped glass are too small to be detected with the measurement accuracy available.

5 Low birefringence waveguides

Current DWDM networks utilize planar lightwave circuits in wavelength routing. These circuits are mainly composed of relatively simple components like directional couplers, Y-branches and filters. In recent years several advanced on-chip integrated optical components for DWDM networks were introduced. These include arrayed waveguide multiplexer/demultiplexers [71], multimode interference couplers [72], optical add/drop multiplexers/demultiplexers [73–76], and header recognition chips for optical packet switching [77]. Most of these components have been demonstrated either in silica-on-silicon platform where fabrication technologies similar to those used in the semiconductor industry can be utilized [76, 78] or in glass substrates using ion-exchanged waveguides [74, 75]. However, these components typically feature an unacceptably high polarization dependence [71, 75]. Since standard single mode fiber is not polarization maintaining, polarization insensitivity in connecting waveguide components is a crucial requirement to be fulfilled in order to avoid polarization dependent performance.

In this work, inherently low birefringence in ion-exchanged waveguides was demonstrated. Special emphasis was put on the effect of birefringence dependence on the waveguide width since many integrated optical components are constructed of waveguides with varying widths. Both even and odd modes were observed to have birefringence of the order of 10^{-5} or below, which is low enough for most telecommunication applications. Low birefringence of both the even and odd mode is of crucial importance in OADMs based on mode conversion [74]. So far, it is one of the only on-chip optical components that has potential to replace fiber-based components utilizing bulky circulators in applications requiring numbers of elements [79, 80].

5.1 Birefringence in ion-exchanged waveguides

When an isotropic material (like glass) is subject to mechanical stress it may become optically anisotropic resulting in stress induced birefringence. Stress can be either compressive or tensile. Typically compressive stress increases the refractive index while tensile stress has the opposite effect [18]. In ion-exchanged waveguides, stress is built in since the exchanged ions have different ionic radii and also because the thermal expansion of the exchanged glass region and the substrate glass are different [17]. In a channel waveguide the stress distribution built up during the waveguide fabrication is unisotropic and has dependence on both x- and y-coordinates:

$$\sigma_x(x,y) \neq \sigma_y(x,y) \neq \sigma_z(x,y), \tag{5.1}$$

where σ_x, σ_y, and σ_z are the stress components along x, y, and z-axis (x-axis being a normal to the surface). Since diffusion has greater ingress in the y-direction than in the x-direction, and because the waveguide can slightly expand along the normal to the surface, the stress component in the x-direction is smaller than in the y-direction ($\sigma_x < \sigma_y$) [17]. The refractive indices for quasi-TE- and quasi-TM-modes depend on the stress components σ_x, σ_y, and σ_z in the following way [17]:

$$n_{TE} = n_0 + C_1\sigma_y + C_2\left(\sigma_x + \sigma_z\right), \tag{5.2}$$

$$n_{TM} = n_0 + C_1\sigma_x + C_2\left(\sigma_y + \sigma_z\right), \tag{5.3}$$

where n_0 refers to refractive index without stress, and C_1 and C_2 are the elasto-optical coefficients of the glass (Note that $C_2 > C_1$ in most glasses [14, 17, 81], and here C_1 and C_2 are taken as positive, therefore for compressive stress $\sigma_y > 0$). It has been observed that in $Ag^+ - Na^+$ ion-exchanged waveguides $n_{TM} > n_{TE}$, indicating compressive stress [17, 82].

Along with stress induced birefringence, the asymmetric refractive index profile of a typical ion-exchanged waveguide also contributes to the waveguide birefringence. This type of birefringence is called form birefringence. Form birefringence produces greater effective refractive index for the quasi-TE mode because the index profile has wider lateral dimensions. In diffused waveguides, form birefringence can be reduced by waveguide burial and/or by thermal annealing that shape the index profile to a more symmetric direction. Burial also reduces the effect of surface on form birefringence, resulting in a more symmetric index profile. In this work (publication III), it is

shown that buried $Ag^+ - Na^+$ ion-exchanged waveguides have inherently low birefringence that can be further reduced by matching form birefringence with the opposite sign stress induced birefringence through thermal annealing. It is also observed that low birefringence can be obtained for a wide range of waveguide widths. This is in contrast to silica-on-silicon waveguides for which low birefringence is attainable only for a rather limited range of waveguide widths [83].

5.2 Low birefringence in buried ion-exchanged waveguides

The waveguides were fabricated into BGG31 glass by molten salt ion exchange as described in Chapter 2 followed by a burial process. Burial was performed for 2400 s at $T = 250°C$ with an applied field of 640 V/mm. Due to the differing self-diffusion coefficients, wider waveguides get buried deeper [84]. With the burial parameters used in fabrication, the depth of the waveguides with mask opening widths from 2 μm to 10 μm varied from 5.6 μm to 6.8 μm.

The waveguide birefringence was defined using a difference interferometer approach described in Ref. [85]. Results before annealing are presented in Fig. 5.1 (crosses). It can be observed from Fig. 5.1 that birefringence for all waveguide widths is low, of the order of 10^{-5} or below. As expected, waveguide birefringence increases as a function of mask opening width, which is mainly due to increasing form birefringence. For all waveguide widths, the effective index of the quasi TE-mode is larger than the effective index of the quasi TM-mode, i.e., $n_{eff,TE} > n_{eff,TM}$.

The effect of annealing on waveguide birefringence is shown in Fig. 5.1. Annealing for 15 min at 250°C reduces the waveguide birefringence only slightly. However, the effect of 45 min total annealing is already significant. Birefringence is of the order of 10^{-6} or below, and interestingly, birefringence for the two narrowest waveguides has changed the sign, meaning $n_{eff,TM} > n_{eff,TE}$. Annealing for another half an hour gives $n_{eff,TM} > n_{eff,TE}$ for all the mask opening widths. Further annealing starts to show signs of saturation, which was expected. As it was explained above, stress-induced birefringence favors higher effective index for TM-mode while form birefringence favors TE-mode. During annealing, ions forming a waveguide diffuse further, and the mode profile becomes more

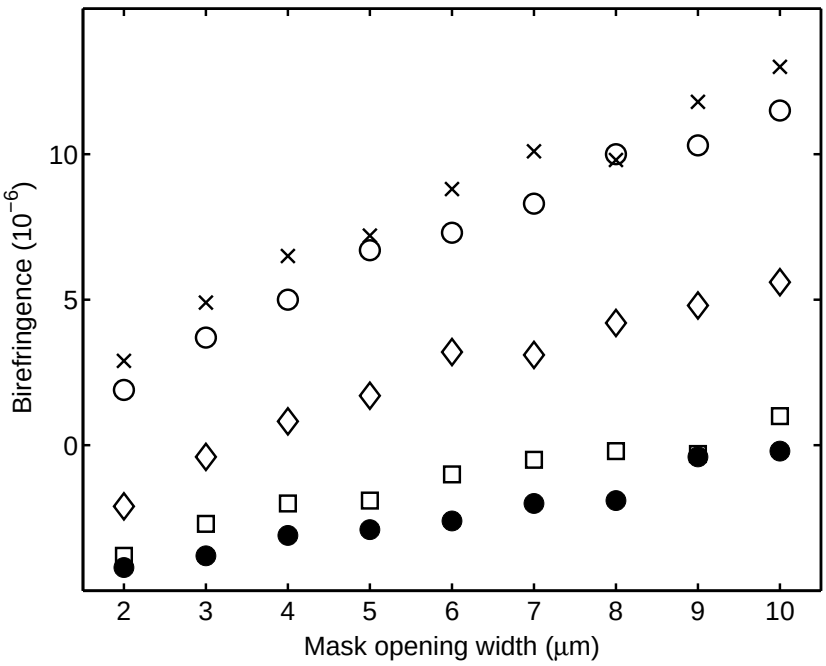

Figure 5.1. Waveguide birefringence ($n_{eff,TE} - n_{eff,TM}$) for different mask opening widths. Crosses refer to waveguides before annealing, open circles to waveguides annealed for 15 min at 250°C, diamonds to waveguides annealed for 45 min, squares to waveguides annealed for 75 min, and filled circles to waveguides annealed for 105 min.

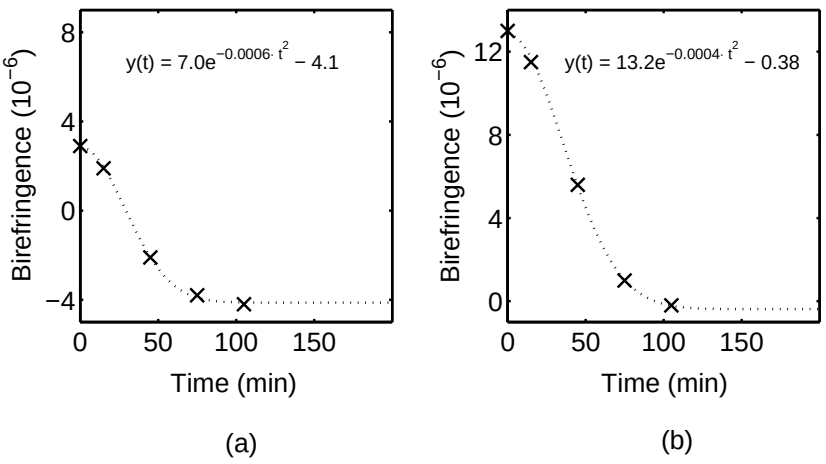

Figure 5.2. Gaussian fits of waveguide birefringence vs. annealing time for waveguides with mask opening widths of (a) 2 μm and (b) 10 μm.

symmetric reducing form birefringence. With long enough annealing, the effect of form birefringence approaches its minimum and the residual birefringence is primarily due to stress-induced effects. Based on the data in Fig. 5.1, birefringence seems to have a Gaussian dependence on annealing time. Values for stress induced birefringence in each individual waveguide were estimated from the saturated values of birefringence through fitting a Gaussian function ($y(t) = a\exp\left(-bt^2\right) + c$, where a, b, and c are fitting parameters) to the data in Fig. 5.1. The results of the fitting are shown in Fig. 5.2. According to the fitting results, birefringence saturates between values of -4.1×10^{-6} and -0.38×10^{-6}. Narrow waveguides show higher residual birefringence than the wider ones. This can be either due to the more pronounced stress-induced birefringence in narrow waveguides or due to higher form birefrigence in wide waveguides. However, the birefringence dependence on waveguide width is less pronounced in case of residual birefringence.

The above results suggest that zero birefringence can be obtained for an individual waveguide if the annealing time is adjusted properly. This might have significance as certain sensor applications require birefringence as low as 10^{-7} [10, 11]. It should be noted that the measurement accuracy is only 1×10^{-6}, therefore a more accurate birefringence measurement method should be used for these sensor applications in order to define the precise annealing time.

5.3 Birefringence of the second order (odd) mode

Integrated optical add-drop multiplexers such as those suggested in Refs. [73–76] require low birefringence not only for the fundamental (even) but also for the second order (odd) mode. This is why it is important to define the second order mode birefringence, too. The results presented here have been studied in more detail in publication IV. The difference interferometric approach utilized in measuring birefringence of the even mode could not be used in case of the odd mode because of the stability issues in coupling the odd mode into the waveguide, therefore, another measurement method was chosen. In this approach, a Bragg grating is utilized in order to measure the slightly different effective refractive indices of the quasi-TE and TM modes. According to the Bragg condition, reflection takes place at wavelengths given by:

$$\lambda = 2n_{eff}\Lambda, \tag{5.4}$$

where λ is the reflected wavelength, Λ is the period of the Bragg grating, and n_{eff} is the effective refractive index of the mode. Each mode has a characteristic effective refractive index, and therefore they are reflected at slightly different wavelengths. The modal birefringence therefore appears as a polarization dependent wavelength (PDW) shift given by

$$\Delta\lambda = 2\Lambda\Delta n_{eff}, \tag{5.5}$$

where $\Delta\lambda = \lambda_{\mathrm{TE}} - \lambda_{\mathrm{TM}}$ is the measured PDW shift, and Δn_{eff} is birefringence to be defined.

The reflected wavelengths for different modes were measured using the setup presented in Fig. 5.3. A broadband light source (ASE) is used to excite simultaneously the modes supported by a waveguide. A fiber circulator couples the light source to the waveguide through ports 1 and 2, and the reflected spectrum is connected to the optical spectrum analyzer (OSA) through port 3. A fiber polarizer (FP) is used to selectively couple either the quasi-TE or -TM polarization state to the waveguide. The power in the unwanted polarization state is minimized by monitoring the transmitted power in this polarization state while tuning the polarization controller (PC). The PDW shift is the wavelength difference between the quasi-TE- and TM-mode reflection peaks. Accuracy of this method is restricted by the OSA resolution and the wavelength repeatability. According to the manufacturer, the OSA (Ando, model AQ6317) used in these measurements has a resolution of 0.015 nm or better and a wavelength repeatability of 0.005 nm,

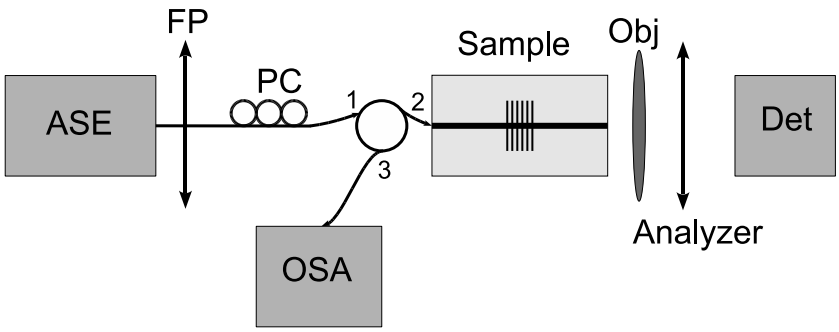

Figure 5.3. A setup for measuring PDW shift.

which is equivalent to a minimum detectable PDW shift of 0.020 nm or better, corresponding to birefringence of 2×10^{-5}. The method described above also includes the possible effect of the grating induced birefringence. Bragg grating is a crucial part in most OADMs [74, 75], and therefore it is important to study if the grating increases polarization sensitivity of the device. Usually UV-exposure induces some birefringence on devices [86, 87]. The effect of the grating induced biregringence was studied by comparing results from two different gratings with reflectivities of 60% and 40%, referred to here as a strong and a weak grating.

The results for even and odd mode birefringence as a function of mask opening width are shown in Figs. 5.4 and 5.5, Fig. 5.4 referring to birefringence with a strong grating and Fig. 5.5 referring to birefringence with a weak grating. It can be seen from Figs. 5.4 and 5.5 that birefringence is below the measurement accuracy of the OSA, i.e., below 2×10^{-5}.

It can be concluded that these ion-exchanged waveguides with birefringence of the order of 10^{-5} or below are suitable for most optical communications applications. It is noteworthy that low birefringence can be obtained for both the even (fundamental) and odd (second order) mode for a wide range of waveguide widths. This result has significance in integrated optical add-drop multiplexers, dispersion compensators, and all-optical packet header recognition chips. This low birefringence for both even and odd modes in a wide range of waveguide widths would be difficult to obtain with other media for integrated optics, such as silica-on-silicon, although birefringence issues have more or less been solved for single mode waveguides. Several approaches to reduce or compensate for birefringence have been suggested in connection with the leading waveguide technology, silica-on-silicon. Typically, these methods include stress tailoring of the cladding layers [88, 89]

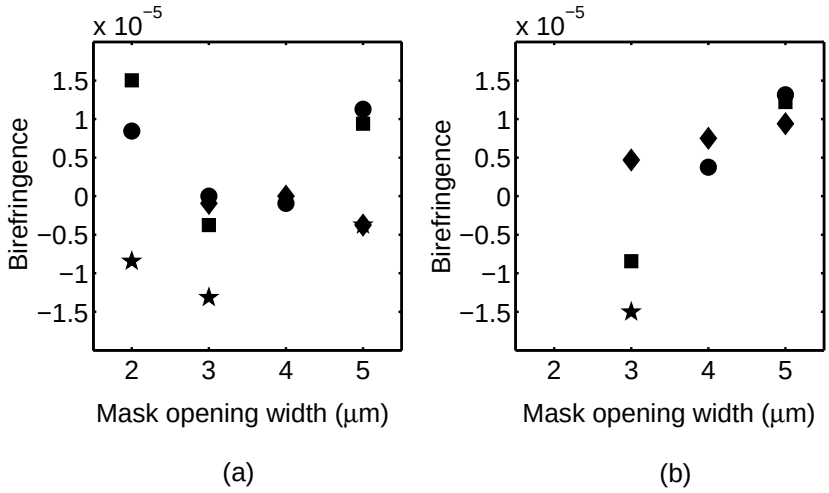

Figure 5.4. Birefringence with a strong waveguide Bragg grating for different mask opening widths. (a) Even and (b) odd mode. Circles, squares, and stars refer to different measurements from waveguides with the same mask opening width.

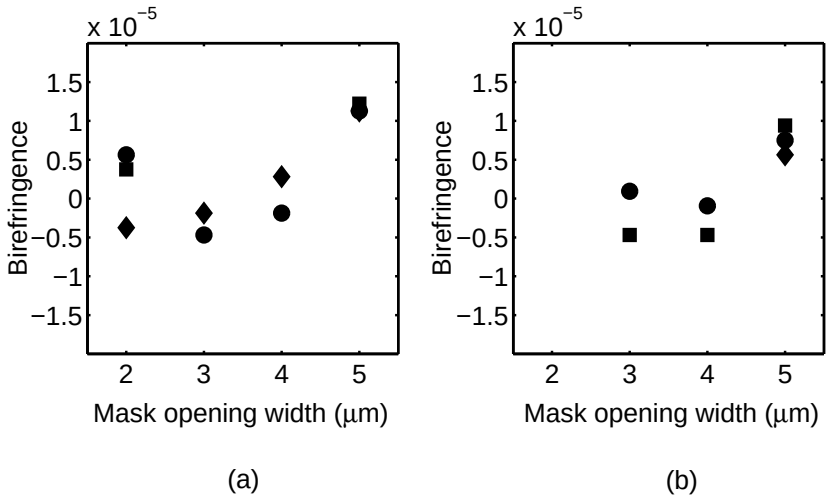

Figure 5.5. Birefringence with a weak waveguide Bragg grating for different mask opening widths. (a) Even and (b) odd mode. Circles, squares, and diamonds refer to different measurements from waveguides with the same mask opening width.

or UV-trimming [90] resulting in waveguide birefringence of the order of 10^{-5} [91]. Stress reduction through etching strain relieving grooves on both sides of the waveguide [78, 92] and integration of birefringence compensating devices into the chip have also been suggested [93]. The major drawback common in all these methods is that they require additional processing steps, and therefore increase the complexity of the device fabrication. Also, this low birefringence for both even and odd modes in a wide range of waveguide widths would be difficult to obtain in silica-on-silicon waveguides [83].

6 Erbium-ytterbium codoped glasses

6.1 Atomic properties of lanthanides

Rare-earth elements are divided into two groups: Lanthanides with an atomic number (Z) between 57 and 71 and actinides with an atomic number between 89 and 103. Lanthanides form a special group among elements. They have a Xenon core structure with full $5s$ and $5p$ shells, the next available shell being the $4f$. Usually the successive electron shells surrounding the atomic nucleus have monotonically increasing radii but in case of lanthanides the outer $4f$ electron shell contracts and becomes bounded by the energetically lower $5s$ and $5p$ shells. This makes lanthanide ions relatively insensitive to the host material, therefore, lanthanide ions in a host material preserve their narrow atomic-like optical spectra with characteristic $4f^N$-$4f^N$ optical transitions [22]. Lanthanides are most commonly available in a trivalent form with the two loosely bound $6s$ electrons and either $5d$ or one of the $4f$ electrons being removed. There are a multitude of states in the $4f$-shell to where electrons can be excited. Unlike in semiconductors and in metals, the localized lanthanide $4f$ wavefunctions result in weak coupling with the crystal vibrations reducing considerably the nonradiative transition rate requiring phonon interaction. All these things make lanthanide ions in a crystal host a favourable choice of material for efficient narrow linewidth lasers. The most common lanthanides used in laser applications are erbium (laser transition at $\sim$ 1535 nm), ytterbium (laser transition at $\sim$ 980 nm and $\sim$ 1064 nm), and neodymium (laser transition at $\sim$ 1064 nm). In fiber optical telecommunication amplifiers, lanthanides deployed include praseodymium ($\sim$ 1300 nm), thulium ($\sim$ 1470 nm), and most commonly erbium (1530 nm -1565 nm). Unlike lasers, optical amplifiers benefit from a broad gain spectrum. The crystal lattice destroys the spherical atomic-

like symmetry and causes splitting of atomic LSJ-multiplets. This is called Stark splitting and it is responsible for the broadening of the gain spectrum in lanthanide doped materials.

6.2 Cross sections

Cross sections describe the capability of an atom or ion to emit or absorb light. Absorption (σ_{12}) or emission (σ_{21}) cross section is a proportionality constant between the absorped/emitted power and the incoming light intensity at a given frequency:

$$P_{abs} = \sigma_{12} I, \tag{6.1}$$

$$P_{em} = \sigma_{21} I. \tag{6.2}$$

Absorption and emission cross sections can be estimated by Einstein's A and B coefficients derived for stimulated emission and absorption, and for spontaneous emission. The probabilities for stimulated emission and absorption and for spontaneous emission depend on the population N_i of the energy level. We can therefore write differential equations describing the emission and absorption phenomena:

$$\left(\frac{dN_2}{dt}\right)_{induced} = -W_{21} N_2, \tag{6.3}$$

$$\left(\frac{dN_1}{dt}\right)_{induced} = -W_{12} N_1, \tag{6.4}$$

and

$$\left(\frac{dN_2}{dt}\right)_{spontaneous} = -A_{21} N_2, \tag{6.5}$$

where $W_{21}^{induced}$ is the transition rate for stimulated emission, $W_{12}^{induced}$ is the transition rate for stimulated absorption and A_{21} is the spontaneous emission rate. In a model proposed by Einstein [40], the induced transition rates between the lower and upper laser levels are both proportional to the photon flux density $\rho(\nu)$ at a frequency ν:

$$W_{21}^{induced} = B_{21} \rho(\nu), \tag{6.6}$$

$$W_{12}^{induced} = B_{12}\rho(\nu), \tag{6.7}$$

where B_{21} and B_{12} are proportionality constants for induced emission and absorption rates. The total downward transition rate is obtained by adding the effect of spontaneous emission:

$$W_{21} = B_{21}\rho(\nu) + A_{21}, \tag{6.8}$$

while the total upward transition rate is that given solely by the induced absorption:

$$W_{12} = B_{12}\rho(\nu). \tag{6.9}$$

Since the magnitude of the proportionality constants B_{21} and B_{12} depends on the atoms or ions, not on the radiation field, Einstein was able to deduce the expressions for B_{21} and B_{12},

$$B_{12} = B_{21}, \tag{6.10}$$

as well as for the spontaneous emission transition rate A_{21},

$$\frac{A_{12}}{B_{21}} = \frac{8\pi n^3 h\nu^3}{c^3}, \tag{6.11}$$

by assuming thermal equilibrium conditions with a blackbody radiation field at (absolute) temperature T given by:

$$\rho(\nu) = \frac{8\pi n^3 h\nu^3}{c^3}\frac{1}{e^{h\nu/kT} - 1}, \tag{6.12}$$

where n is the refractive index of the medium, h is Planck's constant, c is the vacuum speed of light and k is Boltzmann's constant. Einstein's A and B coefficients are linked to the emission and absorption cross sections, σ_{21} and σ_{12}, through equations:

$$\sigma_{21}(\nu) = \frac{h\nu n}{c}B_{21}g_{21}(\nu) = \frac{h}{\lambda}B_{21}g_{21}(\nu), \tag{6.13}$$

$$\sigma_{12}(\nu) = \frac{h\nu n}{c}B_{12}g_{12}(\nu) = \frac{h}{\lambda}B_{12}g_{12}(\nu), \tag{6.14}$$

where $g_{21}(\nu)$ and $g_{12}(\nu)$ are the normalized emission and absorption lineshape functions. Also, the radiative lifetime (reciprocal of the spontaneous emission transition rate) can be given in terms of emission or absorption cross sections in the following way:

$$\frac{1}{\tau_{21}} = A_{21} = \frac{8\pi n^2}{\lambda^2} \int \sigma_{21}(\nu) d\nu = \frac{8\pi n^2}{\lambda^2} \frac{g_1}{g_2} \int \sigma_{12}(\nu) d\nu, \tag{6.15}$$

where λ is the transition wavelength in vacuum and g_1 and g_2 are the degeneracies of the lower and upper laser levels. Equations (6.13)-(6.15) constitute Ladenburg-Fuchtbauer relations and they enable the calculation of the emission cross section and the radiative lifetime through measuring the absorption cross section and the fluorescence spectral profile [22]. Ladenburg-Fuchtbauer relations require that either all the sublevels in a multiplet corresponding to the upper or lower laser level must be equally populated or the transition strengths between the sublevels are all equal, though, in general, this is not the case. For example, in the important case of the lower levels of an erbium ion ($^4I_{13/2}$, $^4I_{15/2}$) the spread in the energy of the sublevels is larger than the thermal energy kT, and in addition, the transition strengths in all glasses are quite sensitive to the Stark levels involved [94]. Thereby, the Ladenburg-Fuchtbauer assumptions are violated and the relations no more provide adequate estimates for the emission cross section. Further improvement to Einstein's model was later introduced by McCumber [95, 96]. McCumber reformulated the Ladenburg-Fuchtbauer relations by making an assumption that the time to establish the thermal equilibrium within the manifold is short compared to the lifetime of that particular manifold, and that the populations of the sublevels obey Boltzmann statistics. The relation between the emission and absorption cross sections according to McCumber theory takes the form:

$$\sigma_{21}(\nu) = \sigma_{12}(\nu) e^{(\epsilon - h\nu)/kT}, \tag{6.16}$$

where ϵ is the mean transition energy between the two manifolds. The radiative lifetime according to McCumber theory becomes

$$\frac{1}{\tau_{21}} = \frac{8\pi n^2}{c^2} \int \nu^2 \sigma_{21}(\nu) d\nu. \tag{6.17}$$

Miniscalco and Quimby [94] demonstrated the validity of the McCumber theory by comparing the emission cross sections calculated according to (6.16) with the exprimentally measured cross sections from Er-doped sil-

ica, silicate, and fluorophosphate glasses. McCumber theory provides absolute values as well as spectral information of the cross sections while the most striking disadvantage of McCumber theory is that it requires knowledge of the electronic structure of the dopant ion, which is usually complicated to obtain. Miniscalco and Quimby introduced a simplified phenomenological procedure to calculate the mean transition energy, ϵ. The cross sections obtained by McCumber analysis are in a good agreement with the experimental results while the Einstein's method overestimates the emission cross section typically by over 25%.

6.3 Lifetime

Excited electrons can decay to lower available states either through radiative (photon-assisted) or nonradiative (phonon-assisted) transition paths. Excited state lifetime is given by:

$$\frac{1}{\tau} = \frac{1}{\tau_r} + \frac{1}{\tau_{nr}}, \tag{6.18}$$

where τ_r and τ_{nr} refer to radiative and nonradiative lifetimes.

The intra $4f^N$ transitions would violate the parity conservation rule and are therefore "forbidden electric dipole" in nature. Consequently the radiative lifetimes in the rare earths tend to be long, on the microsecond or millisecond order [22]. The reason why transitions between $4f^N$ states exist is explained by the presence of a small number of excited opposite parity $4f^{N-1}nl$ configurations [97]. Other mechanisms (low in efficiency) enabling the intra $4f^N$ transitions include magnetic dipole transitions (must satisfy the selection rules) and odd-parity terms in a crystal field Hamiltonian (only for non-centrosymmetric crystals).

Nonradiative transitions require coupling between the lattice vibrations and the rare earth energy states, and are therefore host specific. The transition probability can be linked to the number of phonons required to bridge the energy gap ($m = \Delta E/\hbar\omega$, where ΔE is the energy gap and $\hbar\omega$ is the phonon energy) [98, 99]. The transition probability decreases with the number of phonons required to bridge the gap. As phonons obey Bose statistics, there is also a temperature dependence in the transition probability. Nonradiative lifetime can be expressed as a function of phonon number m and tempera-

ture T:

$$\left(\frac{1}{\tau_{nr}}\right)_{m,T} = \left(\frac{1}{\tau_{nr}}\right)_{m,0} \left[1 - e^{(-\hbar\omega/kT)}\right]^{-m}, \tag{6.19}$$

where $\left(\frac{1}{\tau_{nr}}\right)_{m,0}$ represents the transition rate at zero temperature. Nonradiative transition rate at $T = 0$ decreases exponentially with the number of bridging phonons. The nonradiative transition rate thus becomes:

$$\left(\frac{1}{\tau_{nr}}\right)_{m,T} = Ce^{(-\gamma\Delta E)} \left[1 - e^{(-\hbar\omega/kT)}\right]^{-m}, \tag{6.20}$$

where parameters C and γ are experimentally determined constants.

6.4 Ion-ion interactions and excited state absorption in erbium doped glasses

At high Er^{3+} ion concentrations, the interaction between ions becomes a limiting factor for the amplifier/laser performance. Several effects, including upconversion, excited state absorption (ESA), excitation migration and nonradiative quenching, affect detrimentally the small-signal gain and the pump threshold. These interactions take place because of energy transfer between ions in phonon or virtual photon mediated processes. The order of magnitude of these effects is host specific. Some hosts can incorporate significantly higher concentrations of rare earth ions while other hosts have a greater tendency to form ion clusters therefore providing more possibilities for energy transfer between ions.

The most prevalent upconversion process in Er^{3+} doped glasses is a stepwise upconversion depicted in Fig. 6.1 a. Here, an excited electron transfers its energy to another excited electron in a neighboring ion promoting it to a higher lying state while it simultaneously decays nonradiatively to a lower lying state. In case of Er^{3+} ions, upconversion can take place between two excited electrons either at $^4I_{13/2}$ or $^4I_{11/2}$ level. The upconversion from $^4I_{13/2}$ state reduces the population inversion through reduced radiative lifetime of the level with a consequent increase in the pump threshold and decrease in the small-signal gain. Upconversion from both energy states becomes more significant at high pump powers because the probability for two closely located ions in an excited state increases [22].

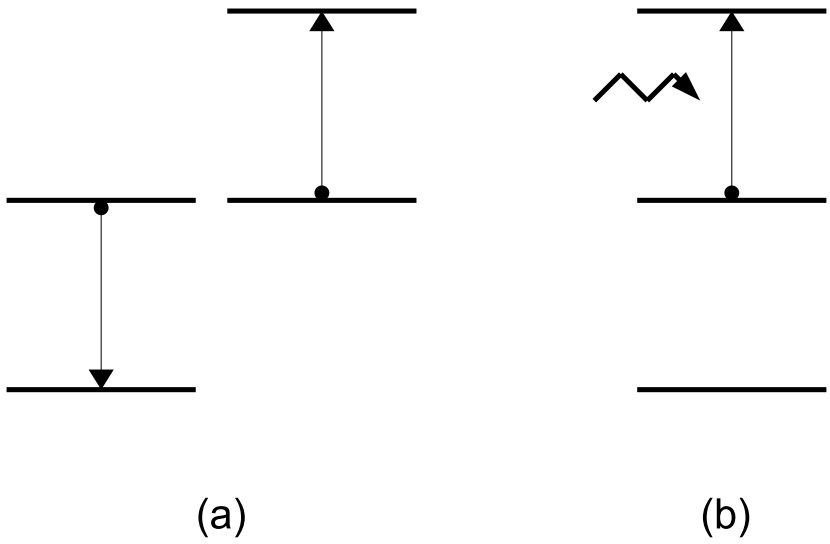

Figure 6.1. Schematics of (a) stepwise upconversion and (b) excited state absorption processes.

The mechanism for ESA is depicted in Fig. 6.1 b. In this process, the electron at $^4I_{13/2}$ state absorbs either a pump or a signal photon futher exciting to $^4S_{3/2}$ or $^4F_{9/2}$ state (in case of 980 pumping). The de-excitation from $^4S_{3/2}$ state is responsible for green light emission in Er^{3+} doped amplifiers and lasers. As well as upconversion, also ESA decreases the maximum gain and the pump efficiency by reducing the population inversion. This effect becomes more pronounced at high pump energies [22].

Other ion-ion interactions worth mentioning are excitation migration and nonradiative quenching. Excitation migration involves neither gain nor loss of energy but may become a limiting factor for the perfomance if the Er^{3+} ion participating in the process is coupled to nonradiative quenching sites. Nonradiative quenching sites are abundant in glasses with high water content (OH-vibration is resonant with the Er^{3+} $^4I_{13/2}$ to $^4I_{15/2}$ transition [100, 101]).

6.5 Optical properties of erbium-ytterbium codoped phosphate glass

The energy levels of an erbium-ytterbium codoped laser system are depicted in Fig. 6.2. Erbium-ion doped glass lasers are often codoped with ytterbium ions since the excited Yb^{3+} ions are able to transfer energy to the ground level Er^{3+} ions. The absorption cross section of Yb^{3+} ions is an order of magnitude higher than the absorption cross section of Er^{3+} ions at the most common pump wavelength of 980 nm [24]. At this wavelength, there are available plenty of inexpensive and efficient single- and multimode diode lasers. The pump wavelength of 980 nm is also more efficient over the 1480 nm pump wavelength because the Er-Yb-codoped laser operates as a three level laser system at this wavelength resulting in higher population inversion.

Phosphate glass has a high solubility of rare-earths compared with more commonly deployed silica and silicate glasses without significant radiative lifetime reduction due to the excited state absorption and up-conversion effects. This enables high gain values in short cavity lengths which is a desirable feature in laser applications. The measured upconversion coefficients (from $^4I_{13/2}$ state) with an erbium concentration of 1×10^{20} cm^{-3} in phosphate glass are of the order of 10^{-18} cm^3/s [24, 102, 103] while those measured from silica and silicate glasses with comparable erbium concentrations are at least an order of magnitude higher [104–106].

As mentioned above, radiative lifetimes are relatively long in rare-earth doped glasses due to the "forbidden electric dipole" nature of the transitions. The lifetime of the $^4I_{13/2}$ level in phosphate glass is approximately 7-8 ms [24, 102, 107] while in silica glasses the lifetime is 10-11 ms [108, 109] and in silicate glasses it is 12-15 ms [22, 108, 110]. The lifetimes of the higher lying levels ($^4I_{11/2}$ and above) are considerably shorter due to the higher nonradiative transfer rates. The phonon energies in lanthanide doped glasses are high to ensure short lifetimes for the higher lying levels. The phonon energy is especially high in phosphate glass resulting in a very short lifetime of 1 μs of the $^4I_{11/2}$ level [110] (in silica glass it is 7 μs [111] and in silicate glass 10 μs [110]). This gives an advantage to phosphate glass in Er-Yb codoped laser systems since it reduces considerably the energy back transfer rate from the Er^{3+} $^4I_{11/2}$ level to the Yb^{3+} $^2F_{5/2}$ level.

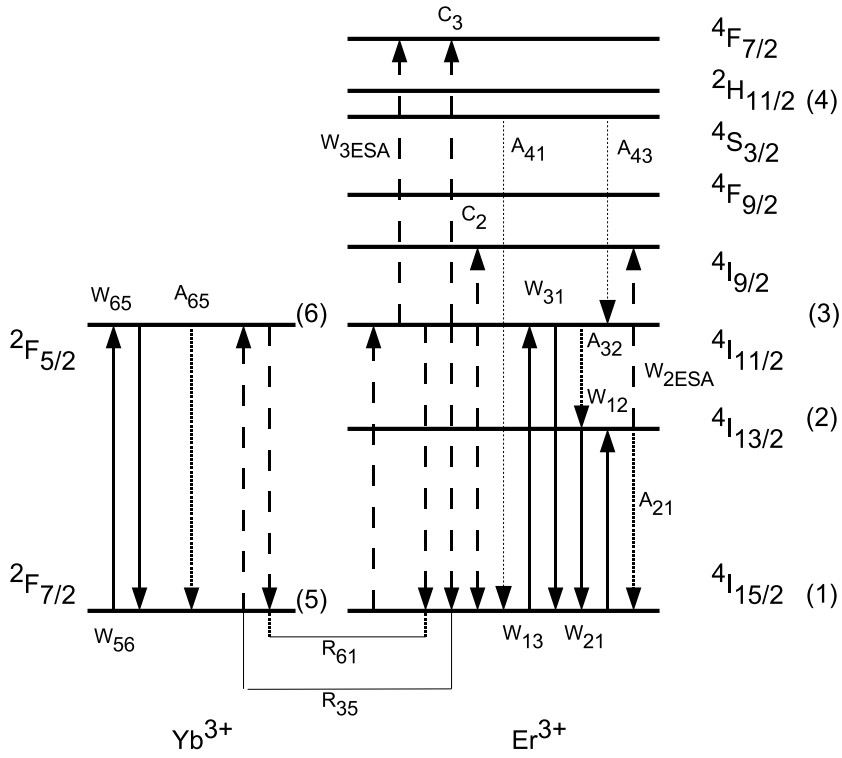

Figure 6.2. A schematic picture of the energy levels of an Er-Yb-codoped laser system. w_{ij} refers to the induced transition rate between the corresponding energy states, A_{ij} refers to the spontaneous emission rate from various states, R_{61} is the energy transfer and R_{35} is the energy back transfer rate between Yb^{3+} and Er^{3+} ions. w_{2ESA} and w_{3ESA} refer to the excited state absorption rate from $^4I_{13/2}$ and $^4I_{11/2}$ states, respectively. C_2 and C_3 refer to up-conversion coefficients from $^4I_{13/2}$ and $^4I_{11/2}$ states.

7 Waveguide lasers

Planar glass waveguide lasers provide some important benefits over widely deployed semiconductor and fiber lasers. The excited state lifetimes of the order of milliseconds in glass materials result in inherently lower noise in waveguide/fiber lasers compared with their semiconductor counterparts having lifetimes of the order of nanoseconds. Higher noise in semiconductor lasers can be associated with their higher spontaneous emission rate. Noise causes undesirable fluctuations in intensity, phase, and center frequency. Phase fluctuations are responsible for the linewidth broadening while intensity fluctuations result in a reduced signal-to-noise ratio (SNR). Thus, due to the longer lifetimes in glass lasers, significantly narrower linewidths can be obtained compared with semiconductor lasers.

In glass lasers relaxation oscillations take place at frequency of ~ 500 kHz whereas in semiconductor lasers relaxation oscillations occur at ~ 1 GHz making relative intensity noise a serious problem in modelocking applications at high repetition rates (above 1 GHz). Lower spontaneous emission rate in glass lasers has also enabled demonstration of modelocked lasers with low timing jitter [112–114]. Timing noise is affected both by frequency noise, which can couple to timing noise through group velocity dispersion, and by intensity noise [115].

In contrast to fiber lasers, waveguide lasers realized on glass substrates allow chip-scale integration of other components, such as pump couplers and power dividers, and enable monolithic integration of multiple optical transmitters at different wavelengths. As discussed in Chapter 6, high gain values can be achieved in waveguides in rare-earth doped phosphate glass substrates. Therefore, waveguide lasers can be made short enabling modelocking at the fundamental round-trip frequency instead of higher harmonics utilized in fiber lasers that easily lead to super-mode or pattern noise problems [116]. A drawback in glass based lasers is that they require optical pumping in contrast to semiconductor lasers that can be pumped electrically. However, Er-Yb-codoped glass waveguide/fiber lasers benefit from

the well-established pump diode lasers developed for the Er-doped fiber amplifiers.

7.1 Short cavity Er-Yb-codoped Ag-Na ion-exchanged waveguide lasers

Several studies have shown that in long haul transmission systems, it is beneficial to use the return-to-zero (RZ) pulse format instead of the non-return-to-zero (NRZ) pulse format since undesirable nonlinear effects can be more easily avoided with the RZ pulse format [117–119]. However, the RZ pulse format is more vulnerable against dispersion due to its larger bandwidth, and also configurations providing the RZ pulse format are more costly, thereby making the NRZ pulse format better in short-distance networks [120]. Compact mode locked lasers operating at 1550 nm region with high repetition rates (10 GHz and above) would provide an ideal, cost-effective RZ pulse source for optical transmitters. Good pulse quality of mode locked lasers improves the signal-to-noise ratio (SNR) enabling scaling to higher repetition rates through optical time division multiplexing (OTDM).

Semiconductor Saturable Absorber Mirrors (SESAMs) provide a compact, cost-effective way to realize mode locking (or Q-switching). Passive, self-starting modelocking of a CO_2 laser by a SESAM was first demonstrated in 1974 by Gibson *et al.* [121]. Since then, SESAMs have been fabricated for wavelengths ranging from the visible to infrared. Pulse repetition rates as high as 160 GHz can be achieved [122]. Pulse durations as short as 6.5 fs have been demonstrated [123] thus approaching the pulse lengths obtained by Kerr lens modelocking [124, 125].

High gain value in short cavity length is a desirable feature in mode locked lasers operating at high pulse frequencies (> 10 GHz) since the cavity length sets the fundamental limit for pulse repetition rate. High small-signal gain also reduces the risk of Q-switching, decreases the mode locking build-up time and enables shorter pulses at steady state [126]. This is why Er-Yb-codoped phosphate glass is an ideal gain-providing medium for mode locked applications at 1550 nm wavelength region. Typical gain values lie between 3–4 dB/cm around 1550 nm wavelengths and in heavily Er-Yb-codoped phosphate glasses, a gain value as high as 4 dB has been measured from only a 3 mm long sample [127]. In phosphate glass, a pulse repetition rate

of 10 GHz is obtained with a cavity length of $\sim$ 1 cm and by shortening the length to $\sim$ 2.5 mm, a pulse repetition rate of 40 GHz can be reached. High repetition rates without Q-switching are difficult to achieve in Er-Yb-codoped glasses because of the small emission cross section of erbium. In spite of this, Zeller *et al.* [128] have demonstrated 40 GHz repetition rates with 4.3-ps-short pulses with careful cavity and SESAM design optimization. The first mode locked waveguide laser was demonstrated by Sclager *et al.* [113] in 2002. They achieved 1-GHz repetition rate with a 2.2-cm long $K^+ - Na^+$ ion-exchanged waveguide in Er-Yb-codoped IOG-1 glass. Passive mode locking was performed by an InGaAs/GaAs multiple-quantum well layer integrated with an AlAs/GaAs thin film stack as a saturable absorber mirror.

In this work (publication V), it was studied whether short cavity Er-Yb-codoped waveguide lasers fabricated by silver-film ion exchange could be utilized as a gain providing element in a SESAM mode locked laser. 1-cm long waveguide laser cavities were fabricated by ion exchange into Er-Yb-codoped IOG-1 glass with mask opening widths between 2 μm and 5 μm. The corresponding mode profiles and dimensions were presented previously in Chapter 3. Samples with three different combinations of Er- and Yb-dopings were tested, and the laser performance of these cavities was measured using a set-up depicted in Fig. 7.1. A fiber-pigtailed single-mode semiconductor diode laser emitting at 980 nm was used as a pump laser. The laser cavity was constructed using a SiO_2/TiO_2 thin film stack as a broadband 1550 nm mirror attached with index matching oil to the waveguide facet while a SiO_2/TiO_2 thin film stack coated straight onto the fiber was used as another mirror. The mirror coated on fiber was transparent at 980 nm and had a reflectance of 93% at 1550 nm wavelength region. Both pump power and output power were coupled in/out through this fiber. A 980/1550 WDM coupler was used to separate pump and output power from each other. Output power was measured by a power meter and the output spectrum of the laser was detected by an optical spectrum analyzer (OSA).

The results are presented in Table 7.1. Output power of 18 mW with a pump laser power of 182 mW was achieved from a multimode Er-Yb-codoped waveguide laser with the best laser performance obtained from a sample with the highest Er^{3+}- and the lowest Yb^{3+}-concentration. The output powers of the two other samples were almost the same while the threshold power was considerably higher for the sample with an Er^{3+}-concentration of 1.25×10^{20} [ions/cm^3] and Yb^{3+}-concentration of 6.0×10^{20} [ions/cm^3]. The measured output powers are not in line with the best gain values measured from the three different samples as high gain value should indicate high

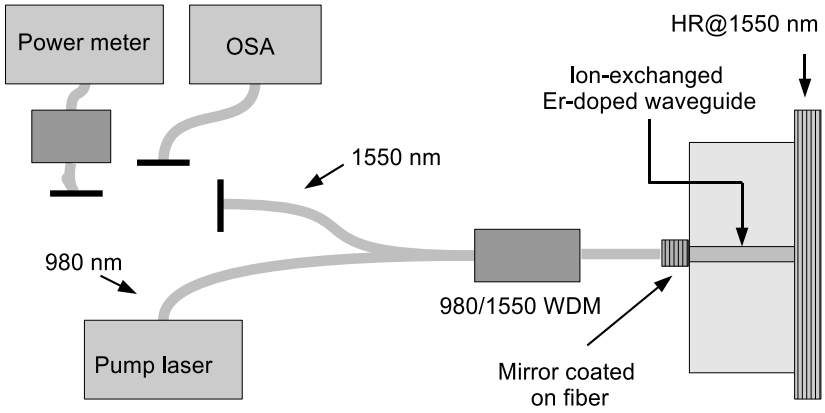

Figure 7.1. A setup for characterizing multimode Er-Yb-waveguide laser cavities.

output power, too. The variation in gain and output powers measured from two identical waveguides in the same sample was significant. It was observed during the measurements that both the gain and the output power values were sensitive to the alignment of the fiber through which pump power was delivered and output power was extracted. It can be therefore concluded that the differences in threshold and output powers as well as in gain values reflect the quality of the fiber alignment, not necessarily differences originating from the differing Er^{3+} and Yb^{3+} concentrations. The results, however, provide an estimate for the output powers available from 1-cm long Er-Yb-codoped waveguide lasers. A significant increase in output power can be expected by optimizing the amount of output coupling.

Similar experiments were carried out by Veasey et al. [24] but with $K^+ - Na^+$ ion-exchanged waveguides. They were able to extract output powers as high as 170 mW from 2.2-cm long samples using a tunable Ti:sapphire laser as a pump laser (pump power ∼610 mW) and an output coupling of 20%. $K^+ - Na^+$ ion-exchanged waveguides have smaller refractive index difference [14], and therefore they are singlemode with wider mask opening widths which, on the other hand, results in bigger mode volumes, and furthermore, higher output powers. However, in modelocking by saturable absorbers, it is the internal intensity that counts. Typical saturation fluence of GaInNAs SESAM (operating at 1.3 μm wavelength region) is 10 $\mu J/cm^2$ [129]. With a typical absorber recovery time of 30 ps, the internal intensity required to saturate the absorber is of the order of 3×10^5 W/cm^2. Considering the output coupling in these lasers was only 7%, the internal

intensity inside the cavity is approximately $3.4 - 5.5 \times 10^5$ W/cm^2 with a typical mode size in a surface waveguide. Therefore, it can be concluded that the 1-cm long Er-Yb-codoped lasers presented in this work would be efficient enough for mode locking applications utilizing GaInNAs SESAMs.

From these experiments, it is obvious that 40 GHz mode locking by GaInNAs SESAMs would require more heavily doped phosphate glass substrates. These kinds of IOG-1 substrates are available and gain values as high as 4 dB have been reached from only 3-mm long samples [127].

Table 7.1. Threshold power, slope efficiency, output power and gain for different erbium and ytterbium concentrations.

$C_{Er^{3+}}$	$C_{Yb^{3+}}$	Threshold	Slope efficiency	P_{out}	Gain
[ions/cm^3]	[ions/cm^3]	[mW]	[%]	[mW]	[dB/cm]
1.5×10^{20}	4.0×10^{20}	130	11	18	3.1
1.0×10^{20}	6.0×10^{20}	154	8	13	3.5
1.25×10^{20}	6.0×10^{20}	170	8	11	4.3

7.2 Waveguide DBR laser with UV-written Bragg grating

Fiber optics technology has greatly benefited from the discovery of photosensitivity of silica-based fibers to UV-irradiation, which enables cost- and time-effective fabrication of Bragg gratings into optical fibers. Fiber Bragg gratings have made it possible to provide dispersion management, filtering, sensing and wavelength control in fibers, and optical feedback in fiber lasers [38]. They have replaced many bulky optical components traditionally used in wavelength multiplexing. Today, fiber Bragg gratings are an essential part of fiber lasers too [130–133].

UV-written Bragg gratings are expected to provide a multitude of opportunities in integrated optics, too. So far, Bragg gratings have been used, e.g., in integrated optical add-drop multiplexers [74] in as discussed in Chapter 5. Use of UV-written Bragg gratings in integrated optical waveguide lasers has

awaited because it has turned out to be difficult to write gratings into glass material that provides enough gain in short cavity lengths (phosphate glass). Conventially, Bragg gratings have been fabricated by a lithographic process that begins with spinning a resist layer on the sample, then patterning it with standard photolithography and finally etching the Bragg grating into glass [24, 134–137]. Another possibility is to use thin-film reflectors grown either straight onto the waveguide facets or attached by some mechanism (e.g. by using index matching oil) onto the waveguide facet. Both of these approaches contain multiple steps in the clean room, and are therefore time-consuming and expensive processes. Clearly, replacing these reflectors by UV-written Bragg gratings would both simplify the fabrication process and improve the laser efficiency (UV-written volume Bragg gratings are nearly lossless and do not couple pump laser light out from surface waveguides).

It was only as recently as 2004 when Pissadakis et al. [138] first demonstrated photosensitivity of Er-Yb-codoped IOG-1 phosphate glass. They fabricated a thin (3 μm-thick) surface-like grating operating in the Raman-Nathan regime by irradiating Er-Yb-codoped IOG-1 glass with KrF excimer laser emitting at 248 nm. UV-irradiation resulted in an index change of 2×10^{-3} in a silver-sodium ion-exchanged sample. Only a small index change of the order of 10^{-5} was observed in a pristine sample. This kind of a surface grating would not work as a mirror in waveguide lasers for two reasons: 1) surface grating at the pump input side would couple out the pump laser power at 980 nm propagating close to the surface, 2) a surface grating with a relatively low index modulation would not provide enough optical feedback for lasing.

In this work (publication VI), it was observed that fabrication of a high quality volume grating in Er-Yb-codoped phosphate glass is indeed a complex task. With improved optical coherence, volume waveguide gratings with maximum reflectance of only 15% were obtained (see Chapter 4). For typical laser applications, however, reflectance above 70% should be obtained, which is why another approach was adopted. As we have seen in Chapter 4, it is possible to write narrow-band high reflectance waveguide gratings into undoped IOG-1 glass. In view of this, we made use of hybrid glass which is a substrate composed of both Er-Yb-codoped and undoped parts bonded to each other [139]. The Bragg grating was written to the undoped part of the hybrid substrate, and it served as a wavelength selective cavity mirror as well as the output coupler of the laser. The Er-Yb-codoped part of the hybrid glass provided the gain required for the laser operation. The Er- and Yb-concentrations were 1.0×10^{20} ions/cm^3 and 6.0×10^{20} ions/cm^3, respectively.

The Bragg grating was written through a phase mask with an ArF pulsed excimer laser. Unlike in the case of the fabrication of the grating with reflectivity of 44% (see Chapter 4), beam expanders were used. This resulted in improved spatial coherence but reduced the fluence to 140 mJ/cm^2. The exposure time was 30 min and the laser was run at a frequency of 100 pps. A phase mask with a period of 1065 nm was designed so that the Bragg grating in IOG-1 glass would have a peak reflectance at 1535 nm corresponding to the gain maximum of Er-doped glass. The waveguide was fabricated after the grating writing.

In Fig. 7.2, the transmission spectra of a 1-cm long waveguide grating for both quasi TE- and TM-polarizations are presented. The transmission minimum occurs at 1534.71 nm (TE) and at 1534.52 nm (TM) with a peak reflectance of 80%. The grating period (533 nm) calculated from the Bragg law corresponds well with the phase mask period divided by two (the theoretical period produced into glass). A polarization dependent wavelength shift of 0.2 nm was observed corresponding to a waveguide birefringence of 10^{-4}. This is not surprising for a surface waveguide in which the proximity of the surface causes more form birefringence than in buried waveguides where birefringence is of the order of 10^{-5} or below (see Chapter 5). A fiber coated with a SiO_2/TiO_2-thin film stack aligned with the waveguide facet in the Er-Yb-codoped part of the substrate was used as another cavity mirror. Pump power from a fiber-pigtailed semiconductor diode laser emitting at 980 nm was also delivered through this fiber. The thin film stack was designed to have transmittance close to 100% at the pump wavelength of 980 nm and reflectance close to 100% at 1550 nm wavelength region.

Since the post-bake annealing could reduce significantly the strength of the UV-written grating, the annealing was performed at 225°C in three steps. After each annealing step, the laser performance was tested. Also the Er-Yb-codoped waveguide length was shortened between the annealing steps. It was deduced from the green light emission (due to ESA) that all available pump power was consumed in a length shorter than the waveguide length in the Er-Yb-codoped part of the substrate, the rest of the Er-Yb-codoped part of the waveguide being underpumped and adding therefore to losses. Shortening the sample increased pump efficiency resulting in improved output power and reduced threshold power. The results between the consecutive annealing steps are shown in Table 7.2. As expected, the threshold power required for lasing steadily decreased with sample annealing and shortening, while the output power and the slope efficiency increased. During annealing, the silver ions diffuse further into glass. Annealing also increases the mode size and smoothens the index profile, therefore reducing

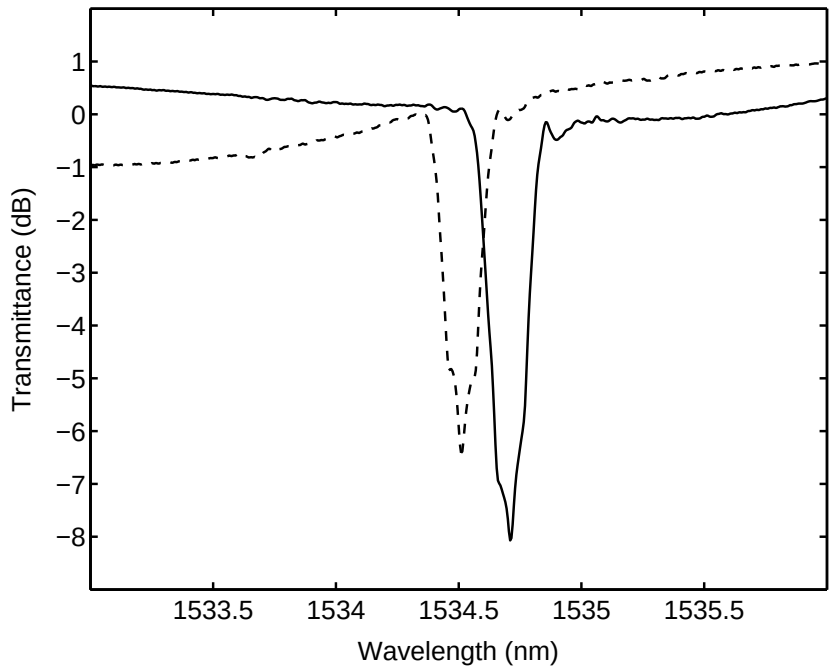

Figure 7.2. Transmission spectra of a UV-written waveguide Bragg grating. The solid line refers to quasi TE-polarization and the dashed line refers to quasi TM-polarization.

coupling and propagation losses. In addition, it improves the mode overlap between the pump and the signal. After the first annealing step, lasing was obtained only when using two pump lasers (the output signal was separated from the pump signal using a 980/1550 WDM-coupler). After the final annealing step, an output power of ~ 9.0 mW could be extracted from the sample with a pump power of 200 mW the threshold being ~ 135 mW. Slope efficiency was 13.9%. The laser output power as a function of pump power is presented in Fig. 7.3. Annealing altogether for 120 min at 225°C did not reduce the grating strength. The lasing wavelength decreased from 1534.77 nm to 1534.50 nm with annealing because the effective index of the propagating mode decreases due to smaller maximum refractive index difference, a characteristic feature of diffused waveguides. In the inset of Fig. 7.3, the laser output spectrum revealing a singlemode operation is presented. The OSA resolution was 0.07 nm. Output power of 9 mW is high enough to provide good SNR but still low enough to avoid undesirable nonlinear effects in optical fibers.

Table 7.2. The effect of shortening and annealing of the sample on threshold and output power, on slope efficiency and lasing wavelength.

Sample length [mm]	Annealing time [min]	P_{pump} (Max) [mW]	P_{out} [mW]	P_{th} [mW]	Slope efficiency [%]	λ_{lasing} [nm]
24	90	315	0.6	260	0.7	1534.77
19	100	200	3.8	148	6.1	1534.71
14	120	200	9.0	135	13.9	1534.50

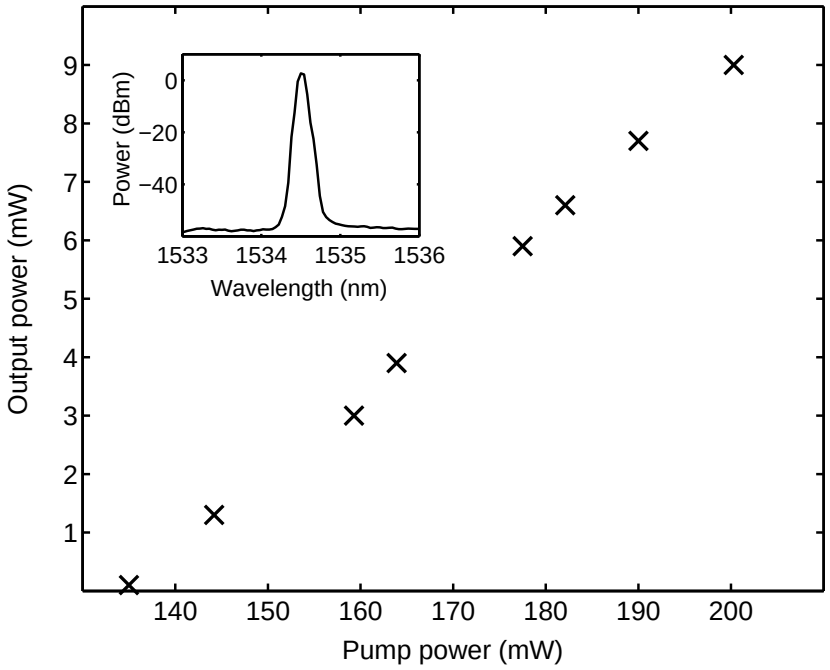

Figure 7.3. DBR laser output power of as a function of pump power. DBR laser utilizes a waveguide Bragg grating as a wavelength selective element as well as another mirror. The laser output spectrum is presented in the inset.

8 Summary

Diffusion parameters (the self-diffusion coefficient of Ag^+ ions and the ratio of self-diffusion coefficients of Ag^+ and Na^+ ions) in IOG-1 phosphate glass have been determined for the silver-film ion exchange process at temperatures 90°C (ion exchange) and 230°C (thermal post-bake). These parameters have significance in designing and modeling waveguide components in IOG-1 glass.

A method for fabricating waveguides with negligible birefringence has been demonstrated. This method includes waveguide burial and thermal post-bake annealing. Low waveguide birefringence has been demonstrated for both fundamental (even) and second order (odd) mode for a wide range of waveguide widths. This approach can be utilized to fabricate waveguide components (such as OADMs) with polarization independent operation.

An extensive study on photosensitivity properties of phosphate glass has been carried out. High quality narrowband waveguide gratings in undoped phosphate glass have been demonstrated. A singlemode waveguide laser utilizing a UV written grating as another mirror was demonstrated in hybrid phosphate glass. The waveguide Bragg grating was written with a pulsed ArF excimer laser emitting at 193 nm. A waveguide grating in Er-Yb-codoped phosphate glass with a reflectivity of 15% has been demonstrated, this time written with a KrF excimer laser emitting at 248 nm. In both cases, the Bragg grating was exposed prior to waveguide fabrication process. It was assumed that silver particles produced during ion exchange prevent UV light from penetrating deep enough into the glass to form a volume grating. This conclusion is supported by the UV-Vis transmission measurements carried out with both pristine and ion-exchanged phosphate glass substrates. However, a thin surface grating with reflectivity of about 12% could be produced in an existing ion-exchanged waveguide. Future work includes developing stronger Bragg gratings in Er-Yb-codoped phosphate glass as this would enable fabrication of compact, narrow linewidth distributed feedback lasers at multiple wavelengths on a single chip.

Short cavity waveguide lasers with multimode operation have been fabricated and characterized. The internal powers obtainable from these 1-cm long Er-Yb-codoped laser cavities are high enough for either Q-switching or modelocking the laser cavity with a semiconductor saturable absorber mirror directly attached to the waveguide facet. These laser cavities have potential to operate as high repetition rate pulsed laser emitters in telecommunication systems. The 1-cm long cavities can produce modelocking at 10 GHz repetition rate. By further reducing the cavity length to 2.5 mm, a 40 GHz repetition rate could be achieved. However, such modelocked laser cavities would require glass substrates with higher doping levels of Er and Yb ions and these kinds of substrates are commercially available. Waveguide Bragg gratings have also potential to improve the pulse quality transmitted by a modelocked laser. Such waveguide gratings could be used to minimize dispersion, and therefore, to obtain pulses with low timing jitter.

References

[1] R. V. Ramaswamy and R. Srivastava, "Ion-exchanged glass waveguides: A review," *J. Lightwave Technol.* **6**, pp. 984–1002, 1988.

[2] A. Hedström, "Ion exchange of ammonium in zeolites: A literature review," *J. Envir. Engrg.* **127**, pp. 673–681, 2001.

[3] M. Streat, ""The waters were made sweet". Advances in ion exchange technology," *Ind. Eng. Chem. Res.* **34**, pp. 2841–2848, 1995.

[4] R. L. Handwerk and R. L. Coleman, "Approaches to the citrus browning problem. A review," *J. Agric. Food Chem.* **36**, pp. 231–236, 1988.

[5] S. Yamamoto, K. Nakanishi, and R. Matsuno, *Ion-Exchange Chromatography of Proteins*, Marcel Dekker Inc., New York, USA, 1988.

[6] N. F. Borrelli, D. L. Morse, R. H. Bellman, and W. L. Morgan, "Photolytic technique for producing microlenses in photosensitive glass," *Appl. Opt.* **24**, pp. 2520–2525, 1985.

[7] S. A. Boppart, T. F. Deutsch, and D. W. Rattner, "Optical imaging technology in minimally invasive surgery," *Surg. Endosc.* **13**, pp. 718–722, 1999.

[8] B. Messerschmidt, B. L. McIntyre, and S. N. Houde-Walter, "Desired concentration-dependent ion exchange for micro-optic lenses," *Appl. Opt.* **35**, pp. 5670–5676, 1996.

[9] A. von Pfeil, B. Messerschmidt, V. Blümel, U. Possner, and T. Possner, "Making fast cylindrical gradient-index lenses diffraction limited by using a wave-front-correction element," *Appl. Opt.* **37**, pp. 5211–5215, 1998.

[10] V. Minier, D. Persegol, J. L. Lovato, and A. Kévorkian, "Integrated optical current sensor with low-birefringence optical waveguides," in

Proceedings of 12th International Conference on Optical Fiber Sensors, Technical Digest, Postconference Edition, *Opt. Soc. America, Washington, USA*, pp. 104–107, 1997.

[11] V. Minier, D. Persegol, J. L. Lovato, G. Clauss, and A. Kévorkian, "Low-birefringence optical waveguides for high performance magneto-optic current sensing," in *8th European Conference on Integrated Optics and Technical Exhibition*, *Proceedings ECIO '97, Opt. Soc. America, Washington, DC*, pp. 94–97, 1997.

[12] G. Gauglitz and J. Ingenhoff, "Integrated optical sensors for halogenated and non-halogenated hydrocarbons," *Sensors and Actuators B* **11**, pp. 207–212, 1993.

[13] T. Izawa and H. Nakagome, "Optical waveguide formed by electrically induced migration of ions in glass plates," *Appl. Phys. Lett.* **21**, pp. 584–586, 1972.

[14] A. N. Miliou, R. Srivastava, and R. V. Ramaswamy, "Modeling of the index change in $K^+ - Na^+$ ion-exchanged glass," *Appl. Opt.* **30**, pp. 674–681, 1991.

[15] J. Albert, "Ion exchange from salt melts," in *Introduction to Glass Integrated Optics*, S. I. Najafi, ed., pp. 7–38, Artech House, Boston, 1992.

[16] N. W. Ashcroft and N. D. Mermin, *Solid State Physics*, Harcort Brace College Publishers, Forth Worth, USA, 1976.

[17] A. Brandenburg, "Stress in ion-exchanged glass waveguides," *J. Lightwave Technol.* **LT-4**, pp. 1580–1593, 1986.

[18] J. Albert and G. L. Yip, "Stress-induced index change for $K^+ - Na^+$ ion exchange in glass," *Electron. Lett.* **23**, pp. 737–738, 1987.

[19] M. Born and E. Wolf, *Principles of Optics*, Cambridge University Press, Cambridge, United Kingdom, 1998 (sixth (corrected) edition).

[20] L. Ross, "Integrated optical components in substrate glasses," *Glastech. Ber.* **62**, pp. 285–297, 1989.

[21] T. Ohtsuki, *Rare-earth doped glass waveguides for amplifiers and lasers*, Ph. D. Thesis, University of Arizona, Tucson, USA, 1996.

[22] P. C. Becker, N. A. Olsson, and J. R. Simpson, *Erbium-Doped Fiber amplifiers: Fundamentals and Technology*, Academic Press, San Diego, USA, 1999.

[23] R. K. Brow, "Review: the structure of simple phosphate glasses," *J. Non-Cryst. Solids* **263&264**, pp. 1–28, 2000.

[24] D. L. Veasey, D. S. Funk, P. M. Peters, N. A. Sanford, G. E. Obarski, N. Fontaine, M. Young, A. P. Peskin, W.-C. L. S. N. Houde-Walter, and J. S. Hayden, "Yb/Er-codoped and Yb-doped waveguide lasers in phosphate glass," *J. Non-Cryst. Solids* **263&264**, pp. 369–381, 2000.

[25] A. Tervonen, "Theoretical analysis of ion-exchanged glass waveguides," in *Introduction to Glass Integrated Optics*, S. I. Najafi, ed., pp. 73–105, Artech House, Boston, 1992.

[26] R. Terai and R. Hayami, "Ionic diffusion in glasses," *J. Non-Cryst. Solids* **18**, pp. 217–264, 1975.

[27] C. F. Gerald and P. O. Wheatley, *Applied Numerical Analysis*, Addison-Wesley Publishing Company, Reading, USA, 1994 (fifth edition).

[28] G. Stewart and P. J. R. Laybourn, "Fabrication of ion-exchanged optical waveguides from dilute silver nitrate melts," *J. Quantum Electron.* **QE-14**, pp. 930–934, 1978.

[29] A. Tervonen, "A general model for fabrication processes of channel waveguides by ion exchange," *J. Appl. Phys.* **67**, pp. 2746–2752, 1990.

[30] S. Honkanen and A. Tervonen, "Experimental analysis of Ag^+-Na^+ ion exchange in glass with Ag film ion sources for planar optical waveguide fabrication," *J. Appl. Phys.* **63**, pp. 634–639, 1988.

[31] K. S. Chiang, "Construction of refractive-index profiles of planar dielectric waveguides from the distribution of effective indexes," *J. Lightwave Technol.* **LT-3**, pp. 385–391, 1985.

[32] K. O. Hill, Y. Fujii, D. C. Johnson, and B. S. Kawasaki, "Photosensitivity in optical fiber waveguides: Application to reflection filter fabrication," *Appl. Phys. Lett.* **32**, pp. 647–649, 1978.

[33] J. Stone, "Photorefractivity in GeO_2-doped silica fibers," *J. Appl. Phys.* **62**, pp. 4371–4374, 1987.

[34] G. Meltz, W. W. Morey, and W. H. Glenn, "Formation of Bragg gratings in optical fibers by a transverse holographic method," *Opt. Lett.* **14**, pp. 823–825, 1989.

[35] D. P. Hand and P. S. J. Russell, "Photoinduced refractive-index changes in germanosilicate fibers," *Opt. Lett.* **15**, pp. 102–104, 1990.

[36] K. O. Hill, B. Malo, F. Bilodeau, D. C. Johnson, and J. Albert, "Bragg gratings fabricated in monomode photosensitive optical fiber by UV exposure through a phase mask," *Appl. Phys. Lett.* **62**, pp. 1035–1037, 1993.

[37] D. Z. Andersson, V. Mizrahi, T. Erdogan, and A. E. White, "Production of in-fibre gratings using a diffractive optical element," *Electron. Lett.* **29**, pp. 566–568, 1993.

[38] J.-L. Archambault and S. G. Grubb, "Fiber gratings in lasers and amplifiers," *J. Lightwave Technol.* **15**, pp. 1378–1390, 1997.

[39] T. Erdogan, "Fiber grating spectra," *J. Lightwave Technol.* **15**, pp. 1277–1294, 1997.

[40] A. Yariv, *Optical Electronics in Modern Communications*, Oxford University Press, New York, USA, 1997 (second edition).

[41] P. W. Milonni and J. H. Eberly, *Lasers*, John Wiley & Sons, New York, USA, 1988.

[42] J. W. Goodman, *Introduction to Fourier Optics*, The McGraw-Hill Companies, Inc., Singapore, 1996 (second edition).

[43] Y. Qiu, Y. Sheng, and C. Beaulieu, "Optimal phase mask for fiber Bragg grating fabrication," *J. Lightwave Technol.* **17**, pp. 2366–2370, 1999.

[44] B. E. A. Saleh and M. C. Teich, *Fundamentals of Photonics*, John Wiley & Sons, Inc., New York, USA, 1991.

[45] K. O. Hill and G. Meltz, "Fiber Bragg grating technology: fundamentals and overview," *J. Lightwave Technol.* **15**, pp. 1263–1276, 1997.

[46] A. Othonos, "Fiber Bragg gratings," *Rev. Sci. Instrum.* **68**, pp. 4309–4341, 1997.

[47] K. O. Hill, F. Bilodeau, B. Malo, T. Kitagawa, S. Thériault, D. C. Johnson, and J. Albert, "Chirped in-fiber Bragg gratings for compensation of optical-fiber dispersion," *Opt. Lett.* **19**, pp. 1314–1316, 1994.

[48] H. Hosono, H. Kawazoe, and J. Nishii, "Defect formation in SiO_2 : GeO_2 glasses studied by irradiation with excimer laser light," *Phys. Rev. B* **53**, pp. R11 921–R11 923, 1996.

[49] R. M. Atkins, V. Mizrahi, and T. Erdogan, "248-nm induced vacuum UV spectral changes in optical fibre preform cores: support for a colour centre model of photosensitivity," *Electron. Lett.* **29**, pp. 385–386, 1993.

[50] D. L. Williams, S. T. Davey, R. Kashyap, J. R. Armitage, and B. J. Ainslie, "Direct observation of UV induced bleaching of 240 nm absorption band in photosensitive germanosilicate glass fibres," *Electron. Lett.* **28**, pp. 369–370, 1992.

[51] L. Dong, J. L. Archambault, L. Reekie, P. S. J. Russell, and D. N. Payne, "Photoinduced absorption change in germanosilicate preforms: evidence for the color-center model of photosensitivity," *Appl. Opt.* **34**, pp. 3436–3440, 1995.

[52] B. Malo, J. Albert, F. Bilodeau, T. Kitagawa, D. C. Johnson, K. O. Hill, K. Hattori, Y. Hibino, and S. Gujrathi, "Photosensitivity in phosphorus-doped silica glass and optical waveguides," *Appl. Phys. Lett.* **65**, pp. 394–396, 1994.

[53] P. J. Lemaire, R. M. Atkins, V. Mizrahi, and W. A. Reed, "Mechanisms of enhanced UV photosensitivity via hydrogen loading in germanosilicate glasses," *Electron. Lett.* **29**, pp. 1234–1235, 1993.

[54] F. Bilodeau, B. Malo, J. Albert, D. C. Johnson, K. O. Hill, Y. Hibino, M. Abe, and M. Kawachi, "Photosensitization of optical fiber and silica-on-silicon/silica waveguides," *Opt. Lett.* **18**, pp. 953–955, 1993.

[55] M. Douay, W. X. Xie, T. Taunay, P. Bernage, P. Niay, P. Cordier, B. Poumellec, L. Dong, J. F. Bayon, H. Poignant, and E. Delevaque, "Densification involved in the UV-based photosensitivity of silica glasses and optical fibers," *J. Lightwave Technol.* **15**, pp. 1329–1342, 1997.

[56] J. Albert, B. Malo, F. Bilodeau, D. C. Johnson, K. O. Hill, Y. Hibino, and M. Kawasaki, "Photosensitivity in Ge-doped silica optical waveguides and fibers with 193-nm light from an ArF excimer laser," *Opt. Lett.* **19**, pp. 387–389, 1994.

[57] C. Fiori and R. A. B. Devine, "Evidence for a wide continuum of polymorphs in $a - SiO_2$," *Phys. Rev. B* **33**, pp. 2972–2974, 1986.

[58] J. M. Gabriagues and H. Février, "Analysis of frequency-doubling processes in optical fibers using raman spectroscopy," *Opt. Lett.* **12**, pp. 720–722, 1987.

[59] W. Primak and R. Kampwirth, "The radiation compaction of vitreous silica," *J. Appl. Phys.* **39**, pp. 5651–5658, 1968.

[60] W. Primak, "Dependence of the compaction of vitreous silica on the ionization dose," *J. Appl. Phys.* **49**, p. 2572, 1978.

[61] P. Cordier, J. C. Doukhan, E. Fertein, P. Bernage, P. Niay, J. F. Bayon, and T. Georges, "TEM characterization of structural changes in glass associated to Bragg grating inscription in a germanosilicate optical fiber preform," *Opt. Commun.* **111**, pp. 269–275, 1994.

[62] B. Poumellec, P. Guénot, I. Riant, P. Sansonetti, P. Niay, P. Bernage, and J. F. Fayon, "UV induced densification during Bragg grating inscription in $Ge : SiO_2$ preforms," *Opt. Mat.* **4**, pp. 441–449, 1995.

[63] M. Rothschild, D. J. Erlich, and D. C. Shaver, "Effects of excimer laser irradiation on the transmission, index of refraction, and density of ultraviolet grade fused silica," *Appl. Phys. Lett.* **55**, pp. 1276–1278, 1989.

[64] J. Albert, K. O. Hill, D. C. Johnson, F. Bilodeau, S. J. Mihailov, N. F. Borrelli, and J. Amin, "Bragg gratings in defect-free germanium-doped optical fibers," *Opt. Lett.* **24**, pp. 1266–1268, 1999.

[65] N. F. Borrelli, D. C. Allan, and R. A. Modavia, "Direct measurement of 248- and 193-nm excimer-induced densification in silica-germania waveguide blanks," *J. Opt. Soc. Am. B* **16**, pp. 1672–1679, 1999.

[66] N. F. Borrelli, C. Smith, D. C. Allan, and T. P. S. III, "Densification of fused silica under 193-nm excitation," *J. Opt. Soc. Am. B* **14**, pp. 1606–1616, 1997.

[67] J. E. Pemberton, L. Latifzadeh, J. P. Fletcher, and S. H. Risbud, "Raman spectroscopy of calcium phosphate glasses with varying CaO modifier concentrations," *Chem. Mater.* **3**, pp. 195–200, 1991.

[68] G. L. Saoût, P. Simon, F. Fayon, A. Blin, and Y. Vaills, "Raman and infrared study of $(PbO)_x(P_2O_5)_{(1-x)}$ glasses," *J. Raman Spectrosc.* **33**, pp. 740–746, 2002.

[69] J. S. Uppal, J. C. Monga, and D. D. Bhawalkar, "Study of thermal effects in an Nd doped phosphate glass laser rod," *IEEE J. Quantum. Electron* **QE-22**, pp. 2259–2265, 1986.

[70] M. Verhaegen, J. L. Brebner, L. B. Allard, and J. Albert, "Ion implantation-induced strong photosensitivity in high-purity fused silica: Correlation of index changes with VUV color centers," *Appl. Phys. Lett.* **68**, pp. 3084–3086, 1996.

[71] M. K. Smit and C. van Dam, "PHASAR-based WDM-devices: Principles, design and applications," *IEEE J. Select. Topics Quantum Electron.* **2**, pp. 236–250, 1996.

[72] L. B. Soldano, F. B. Veerman, M. K. Smit, B. H. Verbeek, A. H. Dubost, and E. C. M. Pennings, "Planar monomode optical couplers based on multimode interference effects," *J. Lightwave Technol.* **10**, pp. 1843–1850, 1992.

[73] A. Tervonen, S. Honkanen, and S. I. Najafi, "Analysis of symmetric directional couplers and asymmetric mach-zehnder interferometers as 1.30- and 1.55 μm dual-wavelength demultiplexers/multiplexers," *Opt. Eng.* **32**, pp. 2083–2091, 1993.

[74] D. F. Geraghty, D. Provenzano, M. Morrell, S. Honkanen, A. Yariv, and N. Peyghambarian, "Ion-exchanged waveguide add/drop filter," *Electron. Lett.* **37**, pp. 829–831, 2001.

[75] J. M. Castro, D. F. Geraghty, B. R. West, and S. Honkanen, "Fabrication and comprehensive modeling of ion-exchanged Bragg optical add-drop multiplexers," *Appl. Opt.* **43**, pp. 6166–6173, 2004.

[76] J. M. Castro, D. F. Geraghty, B. R. West, S. Honkanen, C. M. Greiner, D. Iazikov, and T. Mossberg, "Optical add-drop multiplexers based on the anti-symmetric waveguide Bragg grating," *Appl. Opt.* **45**, pp. 1236–1243, 2006.

[77] D. F. Geraghty, J. M. Castro, B. West, and S. Honkanen, "All-optical packet header recognition integrated optic chip," *IEEE LEOS 2003 Annual Meeting conference*, pp. 752–753, 2003.

[78] E. Wildermuth, C. Nadler, M. Lanker, W. Hunziker, and H. Melchior, "Penalty-free polarization compensation of SiO_2/Si arrayed waveguide grating wavelength multiplexers using stress release grooves," *Electron. Lett.* **34**, pp. 1661–1663, 1998.

[79] A. V. Tran, W. D. Zhong, R. C. Tucker, and R. Lauder, "Optical add-drop multiplexers with low crosstalk," *IEEE Photon. Technol. Lett.* **13**, pp. 582–584, 2001.

[80] A. E. Willner, D. Gurkan, A. B. Sahin, J. E. McGeehan, and M. C. Hauer, "All-optical address recognition for optically-assisted routing in next generation optical networks," *IEEE Commun. Mag.* **41**, pp. S38–S44, 2003.

[81] D. Heiman, D. S. Hamilton, and R. W. Hellwarth, "Brillouin scattering measurements on optical glasses," *Phys. Rev. B* **19**, pp. 6583–6592, 1979.

[82] J. T. A. Carriere, J. A. Frantz, B. R. Youmans, S. Honkanen, and R. K. Kostuk, "Measurement of waveguide birefringence using a ring resonator," *IEEE Photon. Technol. Lett.* **16**, pp. 1134–1136, 2004.

[83] K. Wörhoff, C. G. H. Roeloffzen, R. M. de Ridder, G. Segno, L. T. H. Hilderink, and A. Driessen, "Tolerance of polarization independent waveguides for communication devices," in *Integrated Optics and Photonic Integrated Circuits*, G. C. Righini and S. Honkanen, eds., *Proc. SPIE* **5451**, pp. 369–380, 2004.

[84] P. Madasamy, B. R. West, M. M. Morrell, D. F. Geraghty, S. Honkanen, and N. Peyghambarian, "Buried ion-exchanged glass waveguides: Burial depth dependence on the waveguide width," *Opt. Lett.* **28**, pp. 1132–1134, 2003.

[85] C. S. W. Lukosz, "Integrated optical interferometer as relative humidity sensor and differential refractometer," *Sensors and Actuators A* **25**, pp. 185–188, 1991.

[86] T. Erdogan and V. Mizrahi, "Characterization of UV-induced birefringence in photosensitive Ge-doped silica optical fibers," *J. Opt. Soc. Am. B* **11**, pp. 2100–2105, 1994.

[87] H. G. Limberger, P.-Y. Fonjallaz, and R. P. Salathé, "Compaction- and photoeleastic-induced index changes in fiber Bragg gratings," *Appl. Phys. Lett.* **68**, pp. 3069–3071, 1996.

[88] H. Takahashi, Y. Hibino, Y. Ohmori, and M. Kawachi, "Polarization-insensitive arrayed-waveguide wavelength multiplexer with birefrigence compensating film," *IEEE Photon. Technol. Lett.* **5**, pp. 707–709, 1993.

[89] M. Okuno, A. Sugita, K. Jinguji, and M. Kawachi, "Birefringence control of silica waveguides on Si and its application to a polarization-beam splitter/switch," *J. Lightwave Technol.* **12**, pp. 625–633, 1994.

[90] J. Albert, F. Bilodeau, D. C. Johnson, K. O. Hill, S. J. Mihailov, D. Stryckman, T. Kitagawa, and Y. Hibino, "Polarisation-independent strong Bragg gratings in planar lightwave circuits," *Electron. Lett.* **34**, pp. 485–486, 1998.

[91] A. Kilian, J. Kirchhof, B. Kuhlow, G. Przyrembel, and W. Wischmann, "Birefringence free planar optical waveguide made by Flame Hydrolysis Deposition (FHD) through tailoring of the overcladding," *J. Lightwave Technol.* **18**, pp. 193–198, 2000.

[92] C. K. Nadler, E. B. Wildermuth, M. Lanker, W. Hunziker, and H. Melchior, "Polarization insensitive, low-loss, low-crosstalk wavelength multiplexer modules," *IEEE J. Select. Topics Quantum Electron.* **5**, pp. 1407–1412, 1999.

[93] H. Takahashi, Y. Hibino, and I. Nishi, "Polarization-insensitive arrayed-waveguide grating wavelength multiplexer on silicon," *Opt. Lett.* **17**, pp. 499–501, 1992.

[94] W. J. Miniscalco and R. S. Quimby, "General procedure for the analysis of Er^{3+} cross sections," *Opt. Lett.* **16**, pp. 258–260, 1991.

[95] D. E. McCumber, "Theory of phonon-terminated optical masers," *Phys. Rev.* **134**, pp. A299–A306, 1964.

[96] D. E. McCumber, "Einstein relations connecting broadband emission and absorption spectra," *Phys. Rev.* **136**, pp. A954–A957, 1964.

[97] J. H. V. Vleck, "The puzzle of rare-earth spectra in solids," *J. Phys. Chem.* **41**, pp. 67–80, 1937.

[98] L. A. Riseberg and H. W. Moos, "Multiphonon orbit-lattice relaxation of excited states of rare-earth ions in crystals," *Phys. Rev.* **174**, pp. 429–438, 1968.

[99] M. J. Weber, "Probabilities for radiative and nonradiative decay of Er^{3+} in LaF_3," *Phys. Rev.* **157**, pp. 262–272, 1967.

[100] Y. Yan, A. J. Faber, and H. de Waal, "Luminescence quenching by OH groups in highly Er-doped phosphate glasses," *J. Non-Cryst Solids* **181**, pp. 283–290, 1995.

[101] E. Snoeks, P. G. Kik, and A. Polman, "Concentration quenching in erbium implanted alkali silicate glasses," *Opt. Mater.* **5**, pp. 159–167, 1996.

[102] T. Ohtsuki, S. Honkanen, S. I. Najafi, and N. Peyghambarian, "Cooperative upconversion effects on the performance of Er^{3+}-doped phosphate glass waveguide amplifiers," *J. Opt. Soc. Am.* **14**, pp. 1838–1845, 1997.

[103] S. Taccheo, G. Sorbello, S. Longhi, and P. Laporta, "Measurement of the energy transfer and upconversion constants in Er-Yb-doped phosphate glass," *Optical and Quantum Electronics* **31**, pp. 249–262, 1999.

[104] E. Delevaque, T. Georges, M. Monerie, P. Lamouler, and J.-F. Bayon, "Modeling of pair-induced quenching in erbium-doped silicate fibers," *IEEE Photon. Technol. Lett.* **5**, pp. 73–75, 1993.

[105] F. D. Pasquale and M. Federighi, "Improved gain characteristics in high-concentration Er^{3+}/Yb^{3+} codoped glass waveguide amplifiers," *IEEE J. Quantum Electron.* **30**, pp. 2127–2131, 1994.

[106] F. D. Pasquale and M. Federighi, "Modelling of uniform and pair-induced upconversion mechanisms in high-concentration erbium-doped silica waveguides," *J. Lightwave Technol.* **13**, pp. 1858–1864, 1995.

[107] S. Taccheo, P. Laporta, S. Longhi, and C. Svelto, "Experimental analysis and theoretical modeling of a diode-pumped Er:Yb:glass microchip laser," *Opt. Lett.* **20**, pp. 889–891, 1995.

[108] W. J. Miniscalco, "Erbium-doped glasses for fiber amplifiers at 1500 nm," *J. Lightwave Technol.* **9**, pp. 234–250, 1991.

[109] G. Nykolak, P. C. Becker, J. Shmulovich, Y. H. Wong, D. J. DiGiovanni, and A. J. Bruce, "Concentration-dependent $^4I_{13/2}$ lifetimes in Er^{3+}-doped fibers and Er^{3+}-doped planar waveguides," *IEEE Photon. Technol. Lett.* **5**, pp. 1014–1016, 1993.

[110] V. P. Gapontsev, S. M. Matitsin, A. A. Isineev, and V. B. Kravchenko, "Erbium glass lasers and their applications," *Optics and Laser Technol.* , pp. 189–196, August 1982.

[111] P. F. Wysocki, J. L. Wagener, M. J. F. Digonnet, and H. J. Shaw, "Evidence and modeling of paired ions and other loss mechanisms in erbium-doped silica fibers," in *Fiber laser sources and amplifiers*, *Proc. SPIE* **1789**, pp. 66–79, 1992.

[112] G. J. Spühler, M. Dymott, I. Klimov, G. Luntz, L. Baraldi, I. Kilburn, P. Crosby, S. Thomas, O. Zehnder, C. Y. Teisset, M. Brownell, K. J. Weingarten, R. Dangel, B. J. Offrein, G. L. Bona, O. Buccafusca, Y. Kaneko, L. Krainer, R. Paschotta, and U. Keller, "40 GHz pulse source with less than 350 fs timing jitter," *Electron. Lett.* **38**, pp. 1031–1033, 2002.

[113] J. B. Schlager, B. E. Callicoat, R. P. Mirin, N. A. Sanford, D. J. Jones, and J. Ye, "Passively mode-locked glass waveguide laser with 14-fs timing jitter," *Opt. Lett.* **28**, pp. 2411–2413, 2003.

[114] A. Schlatter, B. Rudin, S. C. Zeller, R. Paschotta, G. J. Spühler, L. Krainer, N. Haverkamp, H. R. Telle, and U. Keller, "Nearly quantum-noise-limited timing jitter from miniature Er:Yb:glass lasers," *Opt. Lett.* **30**, pp. 1536–1538, 2005.

[115] R. Paschotta, "Noise of mode-locked lasers (part ii): timing jitter and other fluctuations," *Appl. Phys. B.* **79**, pp. 163–173, 2004.

[116] X. Shan and D. M. Spirit, "Novel method to suppress noise in harmonically mode-locked erbium fiber lasers," *Electron. Lett.* **29**, pp. 979–981, 1993.

[117] D. Breuer and K. Petermann, "Comparison of NRZ- and RZ-modulation format for 40 Gb/s TDM standard-fiber systems," *IEEE Photon. Technol. Lett.* **9**, pp. 398–400, 1997.

[118] M. I. Hayee and A. Willner, "NRZ versus RZ in 10-40-Gb/s dispersion managed WDM transmission systems," *IEEE Photon. Technol. Lett.* **11**, pp. 991–993, 1999.

[119] R. Ludwig, U. Feiste, E. Dietrich, H. G. Weber, D. Breuer, M. Martin, and F. Kueppers, "Experimental comparison of 40 Gb/s RZ and NRZ transmission over standard singlemode fiber," *Electron. Lett.* **35**, pp. 2216–2218, 1999.

[120] K. Sato, "Semiconductor light sources for 40-Gb/s transmission systems," *J. Lightwave Technol.* **20**, pp. 2035–2043, 2002.

[121] A. F. Gibson, M. F. Kimmitt, and B. Norris, "Generation of bandwidth-limited pulses from a TEA CO_2 laser using p-type germanium," *Appl. Phys. Lett.* **24**, pp. 306–307, 1974.

[122] L. Krainer, R. Paschotta, S. Lecomte, M. M. K. J. Weingarten, and U. Keller, "Compact Nd : YVO_4 lasers with pulse repetition rates up to 160 GHz," *IEEE J. Quantum Electron.* **38**, pp. 1331–1338, 2002.

[123] I. D. Jung, F. X. Kärtner, N. Matuschek, D. H. Sutter, F. Morier-Genoud, G. Zhang, and U. Keller, "Self-starting 6.5-fs pulses from a Ti:sapphire laser," *Opt. Lett.* **22**, pp. 1009–1011, 1997.

[124] D. H. Sutter, G. Steinmeyer, L. Gallmann, N. Matuschek, F. Morier-Genoud, U. Keller, V. Scheuer, G. Angelow, and T. Tschudi, "Semiconductor saturable-absorber mirror-assisted Kerr-lens mode-locked Ti:sapphire laser producing pulses in the two-cycle regime," *Opt. Lett.* **24**, pp. 631–633, 1999.

[125] R. Ell, U. Morgener, F. X. Kärtner, J. G. Fujimoto, E. P. Ippen, V. Scheuer, G. Angelow, T. Tschudi, M. J. Lederer, A. Boiko, and B. Luther-Davies, "Generation of 5-fs pulses and octave-spanning spectra directly from a Ti:sapphire laser," *Opt. Lett.* **26**, pp. 373–375, 2001.

[126] U. Keller, "Semiconductor nonlinearities for solid-state laser mode-locking and q-switching," in *Nonlinear Optics in Semiconductors II*, E. Garmire and A. Kost, eds., pp. 211–285, Academic Press, 1999.

[127] F. D. Patel, S. DiCarolis, P. Lum, S. Venkatesh, and J. N. Miller, "A compact high-performance optical waveguide amplifier," *IEEE Photon. Technol. Lett.* **16**, pp. 2607–2609, 2004.

[128] S. C. Zeller, L. Krainer, G. J. Spühler, K. J. Weinkarten, R. Paschotta, and U. Keller, "Passively modelocked 40-GHz Er:Yb:glass laser," *Appl. Phys. B* **B76**, pp. 787–788, 2003.

[129] V. Liverini, S. Schön, R. Grange, M. Haiml, S. C. Zeller, and U. Keller, "Low-loss GaInNAs saturable absorber mode locking a 1.3-μm solid-state laser," *Appl. Phys. Lett.* **84**, pp. 4002–4004, 2004.

[130] K. H. Ylä-Jarkko and A. B. Grudinin, "Performance limitations of high-power DFB fiber lasers," *IEEE Photon. Technol. Lett.* **15**, pp. 191–193, 2003.

[131] C. Spiegelberg, J. Geng, Y. Hu, Y. Kaneda, S. Jiang, and N. Peyghambarian, "Single-frequency fiber oscillator with watt-level ouput power using photonic crystal phosphate glass fiber," *J. Lightwave Technol.* **22**, pp. 57–62, 2004.

[132] T. Qiu, S. Suzuki, A. Schülzgen, L. Li, A. Polynkin, V. Temyanko, J. V. Moloney, and N. Peyghambarian, "Generation of watt-level single-longitudinal-mode output from cladding-pumped short fiber lasers," *Opt. Lett.* **30**, pp. 2748–2750, 2005.

[133] A. Schülzgen, L. Li, V. L. Temyanko, S. Suzuki, J. V. Moloney, and N. Peyghambarian, "Single-frequency fiber oscillator with watt-level ouput power using photonic crystal phosphate glass fiber," *Opt. Express* **14**, pp. 7087–7092, 2006.

[134] P. Madasamy, G. N. Conti, P. Pöyhönen, M. M. Morrell, D. F. Geraghty, S. Honkanen, and N. Peyghambarian, "Waveguide distributed Bragg reflector laser arrays in erbium doped glass made by dry Ag film ion exchange," *Opt. Eng.* **41**, pp. 1084–1086, 2002.

[135] P. Madasamy, S. Honkanen, D. F. Geraghty, and N. Peyghambarian, "Single mode tapered waveguide laser in Er-doped glass with multimode-diode pumping," *Appl. Phys. Lett.* **82**, pp. 1332–1334, 2003.

[136] D. L. Veasey, D. S. Funk, N. A. Sanford, and J. S. Hayden, "Arrays of distributed-Bragg-reflector waveguide lasers at 1536 nm in Yb/Er codoped phosphate glass," *Appl. Phys. Lett.* **74**, pp. 789–791, 1999.

[137] S. Blaize, L. Bastard, C. Cassagnètes, and J. E. Broquin, "Multiwavelengths DFB waveguide laser arrays in Yb-Er codoped phosphate glass substrate," *IEEE Photon. Technol. Lett.* **15**, pp. 516–518, 2003.

[138] S. Pissadakis, A. Ikiades, P. Hua, A. K. Sheridan, and J. Wilkinson, "Photosensitivity of ion-exchanged Er-doped phosphate glass using 248nm excimer laser radiation," *Opt. Exp.* **12**, pp. 3131–3136, 2004.

[139] S. D. Gonzone, J. S. Hayden, D. S. Funk, A. Roshko, and D. L. Veasey, "Hybrid glass substrates for waveguide device manufacture," *Opt. Lett.* **26**, pp. 509–511, 2001.

ISBN 978-951-22-8755-0
ISBN 978-951-22-8756-7 (PDF)
ISSN 1795-2239
ISSN 1795-4584 (PDF)